Coupling numerical models of deltaic wetlands with AirSWOT, UAVSAR, and AVIRIS-NG remote sensing data

Luca Cortese[1], Carmine Donatelli[1,2], Xiaohe Zhang[1], Justin A. Nghiem[4], Marc Simard[3], Cathleen E. Jones[3], Michael Denbina[3], Cédric G. Fichot[1], Joshua P. Harringmeyer[1], and Sergio Fagherazzi[1]

[1]Department of Earth and Environment, Boston University, Boston, MA, USA
[2]Department of Civil, Architectural and Environmental Engineering, University of Texas at Austin, TX, USA
[3]Jet Propulsion Laboratory, California Institute of Technology, Pasadena, CA, USA.
[4]Division of Geological and Planetary Sciences, California Institute of Technology, Pasadena, CA, USA.

Correspondence: Luca Cortese (lucacort@bu.edu), Xiaohe Zhang (zhangbu@bu.edu)

Abstract. Coastal marsh survival relies upon to their ability to increase their elevation and offset sea level rise. It is therefore fundamental to realistically model the sediment fluxes between marshes, tidal channels and bays. Traditionally, numerical models have been calibrated and validated using in-situ measurements located in few locations within the domain of interest. These datasets typically provide temporal information but lack spatial variability. This paper explores the potential of coupling

5 numerical models with high resolution remote sensing imagery. Products from three sensors from the recent NASA Delta-X airborne mission are used. UAVSAR provides vertical water level change on the marshland, and was used to adjust the bathymetry and calibrate the water fluxes over the marsh. AirSWOT yields water surface elevation within bays, lakes and channels and was used to calibrate the Chezy bottom friction coefficient. Finally, imagery from AVIRIS-NG provide maps of total suspended solids (TSS) concentration that were used to calibrate sediment parameters of settling velocity and critical

10 shear stress for erosion. Three numerical models were developed at different locations and scales along coastal Louisiana using Delft3D. The coupling enabled a spatial evaluation of model performance not possible using simple point measurements. Some limitations were highlighted in the remote sensing imagery and the numerical models that need to be accounted for when comparing the results. Overall, the study shows that calibration of numerical models and their general quality will greatly benefit from remote sensing.

1 Introduction

Coastal marshes are among the most important and functional ecosystems on Earth, as they are able to buffer and protect from storm surges and winds (Farber, 1987; Möller et al., 2014; Haddad et al., 2016; Peter Sheng et al., 2022), store carbon (Saintilan et al., 2013; Nahlik and Fennessy, 2016; Rogers et al., 2019), and offer natural shelter to wildlife (Galbraith et al.,

20 2002; Minello et al., 2003). However, it has been estimated that since the 1900s around 50% of coastal wetlands have been

lost (Nicholls, 2004). The resilience of present coastal wetlands is altered by accelerated sea level rise (Cahoon et al., 2006; Spencer et al., 2016; Schuerch et al., 2018), enhanced subsidence due to groundwater and oil extraction activities (Syvitski et al., 2009), and depleted sediment supply to the coast as a result of extensive river damming (Syvitski et al., 2005). Physically based models are necessary to understand and predict the response of coastal wetlands to such external drivers (Fagherazzi
25 et al., 2020).

In order to determine the evolution of coastal marshes in a climate change scenario, a fundamental step is the quantitative determination of incoming and outgoing sediment fluxes (Ganju et al., 2017). Consequently, it is imperative that numerical models accurately solve the hydrodynamic and sediment transport processes in the coastal area. Currently, in order to calibrate and validate physical models of coastal marshes, scientists use one or multiple stations that measure one or more local quantities
30 such as water levels, temperature, salinity, and sediment concentration in the same location for a prolonged time. This approach is shared by modelling studies that focus solely on hydrodynamics (e.g., Dietrich et al. (2011); Bunya et al. (2010); Defne and Ganju (2015)) and studies that include sediment transport (e.g., Castagno et al. (2018); Zang et al. (2018); Zhang et al. (2019)). In most cases, the instrumentation is installed in a few locations either in open sea, or along the coastline, or within tidal channels and creeks, as sensor installation becomes challenging in the shallow areas of coastal marshes where boat access is
35 not possible. Furthermore, although they inform about temporal variability, these in-situ measurements only provide limited spatial information across the landscape. Consequently, it is challenging to fully evaluate the quality of the simulations over the marsh platform, which is troublesome, given the importance of capturing the flux of water and sediment there. Despite recent progress in this direction, there remains a need to include the extended information provided by remote sensing imagery in numerical models (Fagherazzi et al., 2020).

40 Over time, the introduction of more advanced sensors has improved the spatial resolution of available remote sensing imagery. Coarser resolution sensors, including the Moderate Resolution Imaging Spectroradiometer (MODIS) and NOAA Advanced Very High Resolution Radiometer (AVHRR) have been widely used in various applications for wetlands studies. MODIS data have the advantage of providing near daily coverage of the Earth's surface, but with a resolution of 250 or 500 m depending on the selected band (Pflugmacher et al., 2007). MODIS data timeseries have been used to monitor wetland
45 cover (Tana et al., 2013), estuarine vegetation succession and tidal flat elevation (Zhao et al., 2009), tidal wetlands biophysical characteristics (Ghosh et al., 2016), hurricane disturbance to coastal vegetation (Wang and D'Sa, 2009), and coastal wetland biomass (Lumbierres et al., 2017). MODIS data have also been coupled with tower-based flux measurements to determine the carbon budget and the Gross Primary Production in estuarine and coastal wetlands (Yan et al., 2008; Kang et al., 2018). Similarly to MODIS, AVHRR provides global imagery twice a day, but with a 1km resolution. AVHRR data applications vary
50 from assessing hurricane damage in wetlands (e.g., Ill et al. (1997)) to NDVI seasonal pattern in deltaic systems (e.g., Zoffoli et al. (2008)).

Moderate spatial resolution sensors, with spatial resolution of tens of meters, provide much higher detail of the Earth's surface compared to MODIS and AVHRR. Among them, data provided by the Landsat and Sentinel sensors have been more often used to monitor coastal wetlands compared to other sensors such as the Advanced Spaceborne Thermal Emission and
55 Reflection Radiometer (ASTER), China & Brazil Earth Resource Satellite (CBERS), Systeme Probatoire D'Observation De

La Terre (SPOT 1-4) and Advanced Land Observing Satellite (ALOS) (Guo et al., 2017). Long-term Landsat timeseries have been used to detect coastal wetlands cover and area change (Cardoso et al., 2014; Couvillion et al., 2017; Kaplan and Avdan, 2017; Wang et al., 2019, 2020), wetlands vegetation classification and change (Zhang et al., 2011; Muro et al., 2016; Lopes et al., 2019; Thomas et al., 2019; Balogun et al., 2020; Zhang et al., 2022c), extreme events impact on vegetation (Rodgers
60 et al., 2009), coastal wetland soil vertical accretion rates (Jensen et al., 2022), coastal wetland above ground biomass (Tan et al., 2003; Chen et al., 2022).

Remote sensing studies have also developed algorithms to infer water quality indicators in coastal waters near wetlands (McClain and Meister, 2012). For instance, Fichot et al. (2016) used high resolution remote-sensing reflectance data from the airborne Portable Remote Sensing Spectrometer (PRISM) to derive maps of turbidity, dissolved organic carbon and chlorophyll-a
65 in the San Francisco Bay-Delta Estuary. Jensen et al. (2019) used high resolution remote-sensing reflectance data from NASA's Airborne Visible/Infrared Imaging Spectrometer-Next Generation (AVIRIS-NG) and derived maps of total suspended solids in the waters of the Atchafalaya basin along the Louisiana coast (USA). Other studies utilized operational satellite sensors with coarser spatial resolution and fewer spectral bands to derive sediment concentration in coastal waters. Dorji and Fearns (2016) applied multiple algorithms to MODIS and Landsat imagery in regional waters of northern Western Australia, whereas Zhang
70 et al. (2020) adopted Landsat-8 and Sentinel-2 imagery to derive suspended sediment concentration in Plum Island Estuary in Massachusetts (USA).

High quality optical imagery is limited to cloud-free conditions, therefore remote sensing techniques can also rely on radar sensors to overcome this limitation (Henderson and Lewis, 2008). The ALOS Phased Array L-band Synthetic Aperture Radar (PALSAR), European Remote Sensing satellite (ERS-1), RadarSAT, Advanced Synthetic Aperture Radar (ASAR), Japanese
75 Earth Resources Satellite 1 (JERS-1), Airborne Synthetic Aperture Radar (AIRSAR), and TerraSAR-X are some examples of radar sensors used to monitor wetlands (Guo et al., 2017). Slatton et al. (2008) showed that changes in the multi-polarization L-band AIRSAR backscatter were able to detect herbaceous vegetation in marshes, while Kwoun and Lu (2009) used SAR data over the Louisiana coastal zone to characterize seasonal variations of radar backscattering according to vegetation type, showing that SAR can be adopted to monitor changes in coastal wetland vegetation cover. Within the last decade it was
80 demonstrated that repeat-pass radar interferometry from spaceborne instruments enables measurements of water level change within marshes (Wdowinski et al., 2008; Liao et al., 2020; Xie et al., 2013; Hong and Wdowinski, 2014). This new technology enables direct observation of large scale flow patterns that can only be observed with remote sensing.

In this study, the aim is to showcase the coupling between numerical modelling and high-resolution remote sensing imagery. In particular, it shows that the calibration of hydrological and sediment transport models can be performed with remote sensing
85 data. To do so, multiple remote sensing products from the NASA Delta-X mission are used and three Delft3D numerical models are developed at different spatial resolutions. The paper is structured in the following sections: an introduction to the Delta-X mission and related remote sensing products, set-up of the numerical models, results, and discussion of advantages and limitations of using these datasets with numerical models.
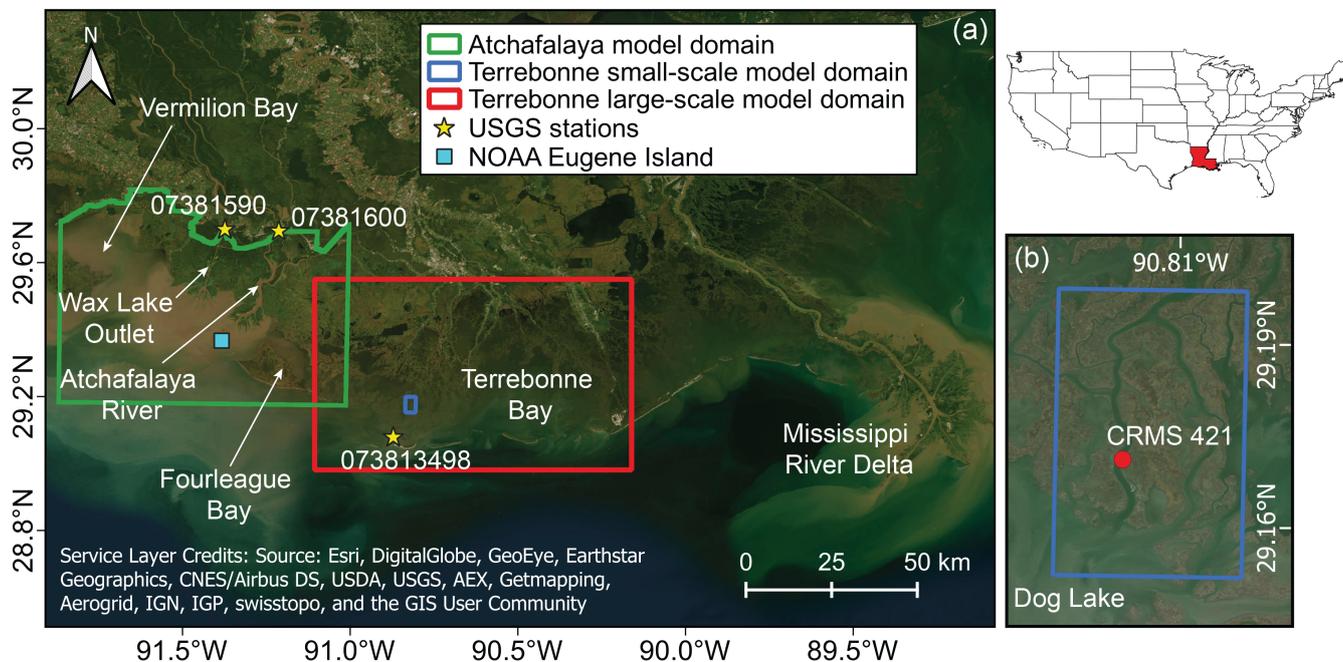
Figure 1. (a) The domains for the Atchafalaya and Terrebonne basin numerical models. The top left inset shows a map of the contiguous US with the state of Louisiana colored in red. (b) Inset showing a detail of the small-scale model domain in the Terrebonne basin. Sources for satellite in Figure 1b are: Esri, DigitalGlobe, GeoEye, Earthstar Geographics, CNES/Airbus DS, USDA, AEX, Getmapping, Aerogrid, IGN, IGP, swisstopo, and the GIS User Community.

2 Methods

2.1 Study area and models domains

90

The Terrebonne and Atchafalaya basins are two neighboring coastal basins located along the Louisiana coast, to the west of the Mississippi River birdfoot delta (Figure 1). Among all basins in the Mississippi River Delta Plain (MRDP), the Terrebonne wetlands have seen the highest rate of areal loss since 1932 (Couvillion et al., 2017; Jensen et al., 2022) due to the lack of sediment load from inland waters. Furthermore, because of the microtidal environment, mineral soil accretion heavily relies on

95 wind waves for bottom sediment resuspension and on surges to transport the sediment over the marsh (Cortese and Fagherazzi, 2022). The basin is characterized by a strong salinity gradient, with salt marshes dominated by Spartina alterniflora along the coast, and brackish and fresh marshes located in landward internal areas (Twilley et al., 2019).

The Atchafalaya basin is located west of Terrebonne and includes the Atchafalaya River and the Wax Lake Outlet. Both rivers mirror the seasonal pattern of the Mississippi hydrograph, with peak discharge between January and June and low discharge

100 in September and October (Allison et al., 2000). The two rivers receive around 30% of the Mississippi River flow through the Old River Control floodgate located north of Baton Rouge (Roberts et al., 2003) and have actively growing deltas, representing

a rare instance of land gain along Louisiana's coast (Couvillion et al., 2017). For instance, the Wax Lake Delta has prograded seaward at a 270 m yr^{-1} rate between 1980 and 2002 (Parker and Sequeiros, 2006). In the Atchafalaya basin nearly 80% of the wetlands are freshwater marshes and swamps due to the high freshwater discharge (Twilley et al., 2019). The distribution
105 of the vegetation is heavily regulated by topography and hydroperiod (Bevington and Twilley, 2018).

In order to examine the use of remote sensing to calibrate models at different scales, three numerical models were developed at different scales. The large-scale Terrebonne model (red rectangle in Figure 1) extends longitudinally for 90 km and borders with the Atchafalaya basin to the west. The small-scale Terrebonne model is located within the salt marsh in the south-west portion of Terrebonne (blue rectangle in Figure 1) and is connected to the south with the small Dog Lake. The domain consists
110 of an island surrounded by two main channels with a 100-150 m wide cross section that converge at the northern top of the island. Finally, the Atchafalaya model (green rectangle in Figure 1) extends longitudinally for 84 km and, besides the two deltas, includes Fourleague Bay to the east and Vermilion Bay to the west.

2.2 NASA Delta-X mission

Delta-X is a NASA mission funded by the Science Mission Directorate's Earth Science Division through the Earth Venture
115 Suborbital-3 Program (Simard et al. (2022); https://deltax.jpl.nasa.gov/), which aims to investigate how feedbacks between hydrological and ecological processes enable marshes and deltas to survive relative sea level rise. The project is focused on the two basins of the MRDP introduced above. The mission has produced airborne high-resolution remote sensing imagery and in-situ measurements that can be incorporated in hydrodynamic, sediment transport and ecological numerical models. In 2021, two field campaigns were completed, one in Spring and one in Fall in order to capture the maximum and minimum flood
120 stages of the Mississippi river discharge.

2.3 UAVSAR, AirSWOT, and AVIRIS-NG

During both Delta-X campaigns, three airborne remote sensing instruments repeatedly collected data to capture the hydrology and infer sediment concentration during different tidal stages.

The Uninhabited Aerial Vehicle Synthetic Aperture Radar (UAVSAR) is a fully polarimetric L-band synthetic aperture radar
125 (SAR), with a wavelength of 23.8 cm, installed on a NASA Gulfstream-III aircraft, that can provide highly coherent rapid repeat-pass SAR acquisitions. UAVSAR data provide a measurement of water level change over wetlands with a resolution of 6 m through repeat-pass interferometry, which allows the detection of surface displacement using multiple observations from the same viewing geometry (Rosen et al., 2006). In flooded wetlands, the water surface is detected through the double-bounce scattering mechanism from water and vegetation (Kim et al., 2009; Wdowinski et al., 2013). Figure 2a shows an example of
130 water level change measured on the wetlands in western Terrebonne by UAVSAR between 17:13 and 17:44 (GMT) on 06 April 2021. A phase unwrapping algorithm is employed to convert interferometric phase change $\Delta\phi$ to change in elevation Δz (Oliver-Cabrera et al., 2021). Here, Level-3 UAVSAR data acquired in Terrebonne (Jones et al., 2022) are used.

AirSWOT is an airborne Ka-band synthetic aperture radar with a wavelength of 0.84 cm flown on a Beechcraft King Air B200, that measures water surface elevation and water surface slope in open waters with uncertainty below 0.3 cm/km. Air-

135 SWOT uses cross-track interferometry to measure the elevation and combines it with along-track interferometry to correct for the bias due to the water motion (Goldstein and Zebker, 1987). More details on the application of AirSWOT are reported by Denbina et al. (2019). Figure 2b shows an example of water surface elevation in western Terrebonne acquired along a flight line on 05 April 2021 at 22:22 GMT. Here, Level-2 AirSWOT geocoded water surface elevation data in Terrebonne and Wax Lake (Denbina et al., 2022) are used.

140 The Airborne Visible/Infrared Imaging Spectrometer-Next Generation (AVIRIS-NG) is a high-resolution imaging spectrometer that measures radiance for 432 bands at 5-nm spectral sampling between 380 and 2510 nm (Hamlin et al., 2011). The calibrated radiance measurement from AVIRIS-NG were atmospherically corrected to produce spectral remote-sensing reflectance ($R_{rs}(\lambda)$) of the water, and surface reflectance of the land. Local empirical algorithms derived using in-situ measurements during Delta-X were used to derive TSS concentration form the $R_{rs}(\lambda)$ in the visible/near-infrared region and generate maps of

145 TSS from the AVIRIS-NG imagery and vegetation structure are produced (Gao et al., 1993; Bue et al., 2015; Jensen et al., 2019). AVIRIS-NG images were also used to produce maps of vegetation structure (Jensen et al., 2021). Figure 2c shows an example of total suspended solids (TSS) concentration maps derived from AVIRIS-NG over the Wax Lake Outlet acquired on 02 April 2021 at 20:31 GMT. Here, the AVIRIS-NG Level3-derived TSS data in Terrebonne and Wax Lake are used (Fichot and Harringmeyer, 2022).

150 **2.4 Large-scale Terrebonne model set-up**

The Delft3D model was used to simulate water levels and sediment transport during the Delta-X 2021 Spring campaign. The FLOW module (Lesser et al., 2004) was coupled with SWAN (Simulating Waves Nearshore, e.g. Holthuijsen et al. (1993); Booij and Holthuijsen (1987)) to account for wave resuspension of bottom sediments. The model ran from 25 March 2021 to 18 April 2021 with an additional 5 days as warm-up period. The domain (Figure 1) consisted of 1139×686 cells with a

155 90×90 m resolution. Bathymetric data were referenced to the NAVD88 vertical datum and are available from NOAA (Love et al., 2010). Boundary conditions were water levels imposed at the south boundary in the Gulf of Mexico. Water level data were taken from the United States Geological Survey (USGS) station at Caillou Bay SW of Cocodrie (ID:073813498). The water levels at the boundary were adjusted to reproduce the correct water levels at the USGS station location by shifting the phase and correcting the amplitude to account for signal damping. Data of wind speed and direction were taken from the same

160 USGS station and applied homogeneously on the entire domain with an hourly time resolution. Two sediment types composing the bottom were considered: sand (non-cohesive fraction) and mud (cohesive fraction). The initial sediment distribution were derived from the usSEABED database (Williams et al., 2006), which provides the fraction of mud and sand in each cell.

The model was coupled with AirSWOT to calibrate the bed roughness which is expressed as Chezy coefficient. Three different friction categories were considered: open sea/ocean, tidal channels/lakes/bays, and marsh platform. Since the AirSWOT

165 campaign covers the water area, the calibration of the Chezy coefficient was focused only on the tidal channels/lakes/bays. Values of 50 and 35 $\mathrm{m}^{1/2}\mathrm{s}^{-1}$ were set for ocean and marsh platform respectively, whereas 40, 42.5, and 45 $\mathrm{m}^{1/2}\mathrm{s}^{-1}$ were evaluated for the tidal channels/lakes/bays.
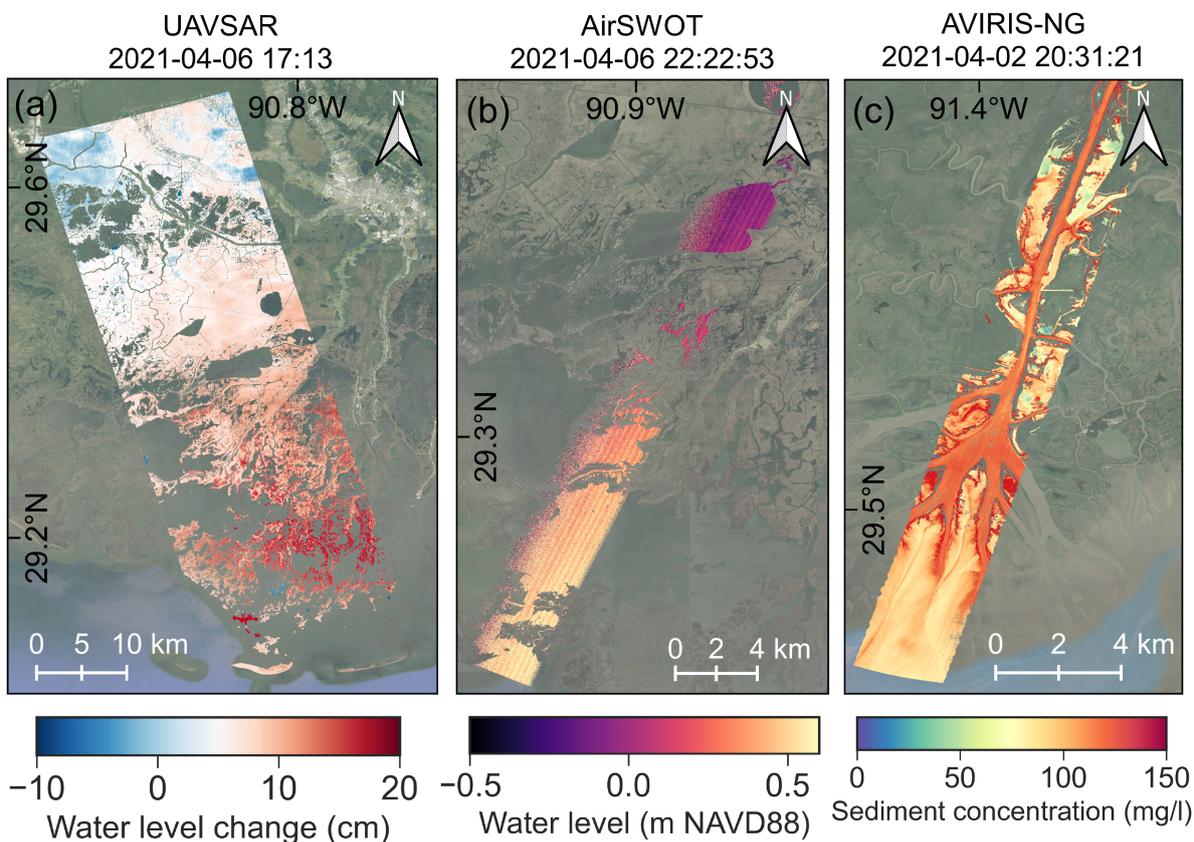
Figure 2. Example of Delta-X remote sensing products. At the top of each map the acquisition time is reported in GMT. (a) Water level change on the marsh from UAVSAR. (b) Water elevation from AirSWOT. (c) Total suspended solids (TSS) concentration derived from AVIRIS-NG.

The model was coupled with AVIRIS-NG to calibrate sediment parameters. Sand density and median diameter (D_{50}) were set to be constant at 2650 kg/m^3 and 0.14 mm, respectively. Note that in the case of non-cohesive particles, Delft3D does not require to specify a value for the settling velocity, since it is directly computed from the median diameter. Thus, the calibration of the parameters refers to the properties of the mud fraction. In Delft3D, the cohesive sediment is defined by density, settling velocity, critical shear stress for erosion/sedimentation, and erosion parameter. In this case, the settling velocity, w_s, and critical shear stress for erosion, $\tau_{cr,e}$, were calibrated. In particular, the last parameter is the threshold above which the applied shear stress is able to entrain bottom sediment. More details on the sediment transport formulation adopted in Delft3D are found in Partheniades (1965) and the Delft3D-FLOW manual. In total, five possible values for w_s (0.1, 0.175, 0.25, 0.325, 0.4 mm/s) and five possible values for $\tau_{cr,e}$ (0.05, 0.075, 0.1, 0.125, 0.15 Pa) were tested.

2.5 Small-scale Terrebonne model set-up

Delft3D was utilized to simulate the hydrodynamics in one of the Delta-X intensive field study sites near CRMS station 421 (blue rectangle in Figure 1) from 25 March 2021 to 18 April 2021. An additional interval of time of 5 days was used as a
180 spin-up period. The numerical grid had a resolution of 10 m and consists of 300×520 cells. Bathymetric information comes from LiDAR, and is given with respect to NAVD88 (Denbina et al., 2020). Boundary conditions were the water levels imposed at the bottom and upper boundaries. The former were the water levels measured by the CRMS site 421, while the latter were computed using water levels measured by CRMS at site 421 and Trouble Bayou. Specifically, a uniform tidal dissipation was assumed between the two stations and used the distance between station 421 and Trouble Bayou and the distance between
185 station 421 and the upper boundary to infer the water levels at the upper boundary. Bottom friction was imposed in terms of Chezy coefficients: 55 $m^{1/2}s^{-1}$ for the channels and 35 $m^{1/2}s^{-1}$ for the marsh platform.

UAVSAR-derived water-level changes were used to correct marsh topography. The methodology proposed by Zhang et al. (2022a) was followed, in which errors in topography were removed by comparing modelled water-level changes with those observed via UAVSAR. This iterative procedure is based on the principle that increasing (decreasing) marsh elevation leads
190 to less (more) tidal propagation, and therefore smaller (greater) water-level changes. In each iteration, we corrected marsh topography based on the difference between observed water-level changes and those obtained via numerical modelling until the numerical solution converged to UAVSAR as close as possible.

2.6 Atchafalaya model set-up

Similar to the large scale model in Terrebonne, a Delft3D-FLOW model was developed to simulate water levels and sediment
195 transport in the Atchafalaya basin (Figure 1) during the Delta-X 2021 Spring campaign. The model had 927×787 cells with a 90x90 m resolution. The model ran from 15 March 2021 to 25 April 2021. Bathymetric data was referenced to NAVD88 (Denbina et al., 2020). The model had a total of three imposed boundary conditions. Water discharge from the USGS station at Calumet (ID: 07381590) was imposed for the Wax Lake Outlet, while water discharge from the USGS station at Morgan City (ID: 07381600) was imposed for the Atchafalaya River. The two stations also provided suspended sediment data that were
200 imposed as boundary conditions for the sediment transport model. Water levels from the NOAA station at Eugene Island (ID: 8764314) are used to set the oceanic boundary. Since the oceanic boundary is located further offshore, we adjusted the signal using the same procedure described in the Terrebonne large scale model. Hourly wind speed and direction data were retrieved from the same station and applied uniformly over the domain.

Three categories were considered for the bed friction calibration with AirSWOT. The Chezy coefficient was fixed at 35
205 $m^{1/2}s^{-1}$ for the marsh, and 8 $m^{1/2}s^{-1}$ for the forest (Zhang et al., 2022a). The evaluated values for open water friction were 45, 55, and 65 $m^{1/2}s^{-1}$.

For sediment transport, three sediment types composing the bottom: sand, silt, and mud were considered. The initial sediment distribution was derived from the usSEABED database and set at 22% sand, 39% silt, and 39% clay. Settling velocities for silt and clay were fixed at 1 mm/s and 0.5 mm/s, respectively, while the median diameter of sand was set at 0.1 mm. AVIRIS-NG

Table 1. Calibrated parameters and relative remote sensing data used for each model.

Model	Calibrated parameter	Remote sensing data used
Large scale Terrebonne	C_h / w_s, $\tau_{cr,e}$	AirSWOT/AVIRIS-NG
Small scale Terrebonne	Bathymetry	UAVSAR
Atchafalaya	C_h / $\tau_{cr,e}$	AirSWOT/AVIRIS-NG
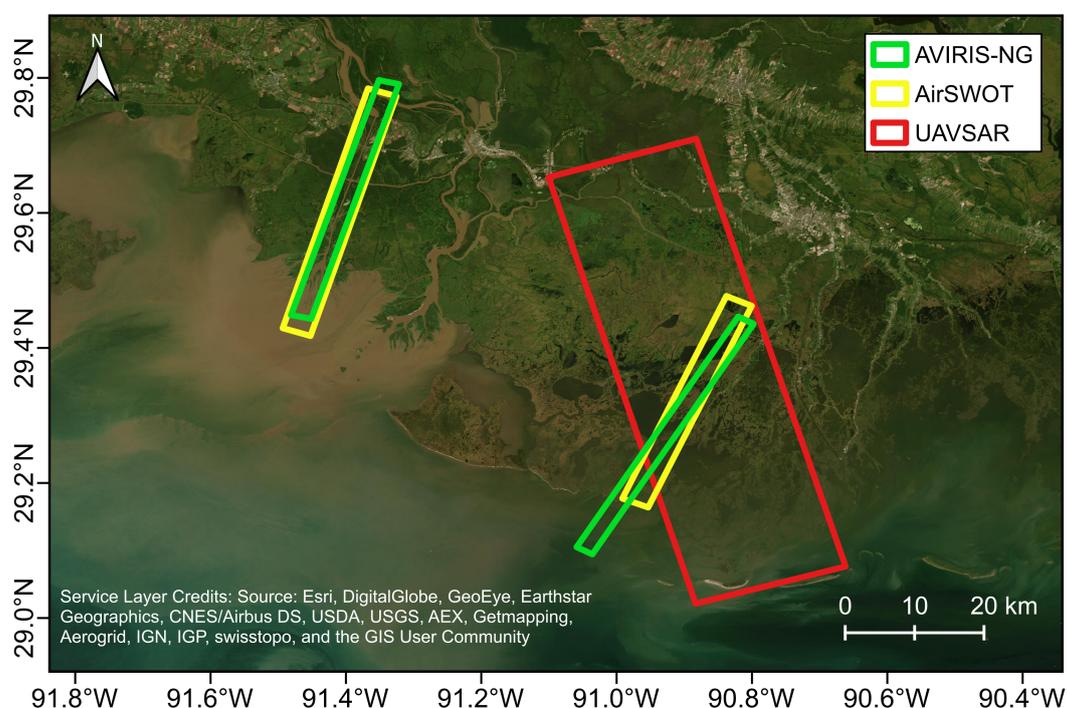
Figure 3. Extension of the flight lines used in this study. The location of Caillou Lake is also indicated.

210   sediment concentration maps were used to calibrate the critical shear stress for erosion. Evaluated values were 0.025, 0.03, 0.04. 0.05, 0.1 Pa for clay, and 0.05, 0.1, 0.2 Pa for silt. For this model, performance of the sediment transport model was also evaluated with and without waves, which were computed with SWAN.

2.7   Coupling between imagery and numerical model

Table 1 summarizes the calibrated parameters for each model and the correspondent remote sensing data used, while Figure 3
215   shows the chosen flight lines of the three instruments.

     In all three models, the coupling between remote sensing images and model allowed to tune models parameters to best match models outputs and the observation. Water levels and sediment concentration from the numerical models were extracted

using the spatial extent of the chosen flight lines and overlapped to enable comparisons. The comparison was first performed visually, in order to identify evident discrepancies. Then, a pixel-by-pixel comparison was performed to better quantify model

220 performance. For the Terrebonne large scale model and Atchafalaya model, because of the 90 m mesh resolution, both Air-SWOT and AVIRIS-NG resolution was lowered by averaging values within a 90 m pixel. The evaluation of the models was performed by computing the error as the difference between the measurement and the modelled value, with a positive error indicating underestimation. The root mean square error (RMSE) was adopted as a global metric in order to compare the overall performance of each simulation. Parameter values providing the lowest RMSE were identified as the optimal ones.

225 For the large scale Terrebonne model, a validation of the outputs was performed following the calibration. Water levels were compared with the timeseries of 13 stationary gauges within the Coastwide Reference Monitoring System (CRMS) network distributed across the domain.

3 Results

3.1 Coupling with AirSWOT

230 For the Terrebonne large scale model, results of simulations with Chezy values of 40 and 45 $\mathrm{m}^{1/2}\mathrm{s}^{-1}$ are shown for four acquisitions of the same flight line at different times during the tidal cycle (Figure 4). The flight line has south-west to north-east direction. At the bottom, it crosses a channel with a 500-700 m cross-section and one of the major lakes in Terrebonne (Caillou Lake). At the top, it intersects a portion of other lakes and small channels. With the exception of the last acquisition on 07 April (Figure 4D) where similar results were found independently from the friction coefficient, a Chezy coefficient of

235 45 $\mathrm{m}^{1/2}\mathrm{s}^{-1}$ allows the model to better match the AirSWOT observations (see also Figure S1). In all cases, the model displays better agreement in the bottom section of the flight line, whereas the discrepancy between remote sensing data and model results tends to increase in the top section. In particular, in the north-most portion, the model always overestimates water elevation.

The validation of the model with C_h = 45 $\mathrm{m}^{1/2}\mathrm{s}^{-1}$ using timeseries reveals temporal coherence between data and modelled

240 values good, with an RMSE of 0.067 m (see Figures S1 and S2, and Table S1).

For the Atchafalaya model results of simulations with Chezy values of 45 $\mathrm{m}^{1/2}\mathrm{s}^{-1}$ and 65 $\mathrm{m}^{1/2}\mathrm{s}^{-1}$ (Figure 5 and S2) are shown focusing on the Wax Lake Delta. A Chezy coefficient of 65 $\mathrm{m}^{1/2}\mathrm{s}^{-1}$ drastically improves model performance compared to the 45 $\mathrm{m}^{1/2}\mathrm{s}^{-1}$ case, with a reduction of the RMSE from 25.6 cm to 14.3 cm. In particular, the reduction of bottom friction allows the model to better represent water elevations in the main channel, but especially in the vicinity of the

245 distributary channels of the delta where the model with 45 $\mathrm{m}^{1/2}\mathrm{s}^{-1}$ tends to overestimate the water elevations. Furthermore, the 65 $\mathrm{m}^{1/2}\mathrm{s}^{-1}$ is able to detect the west-to-east surface slope.
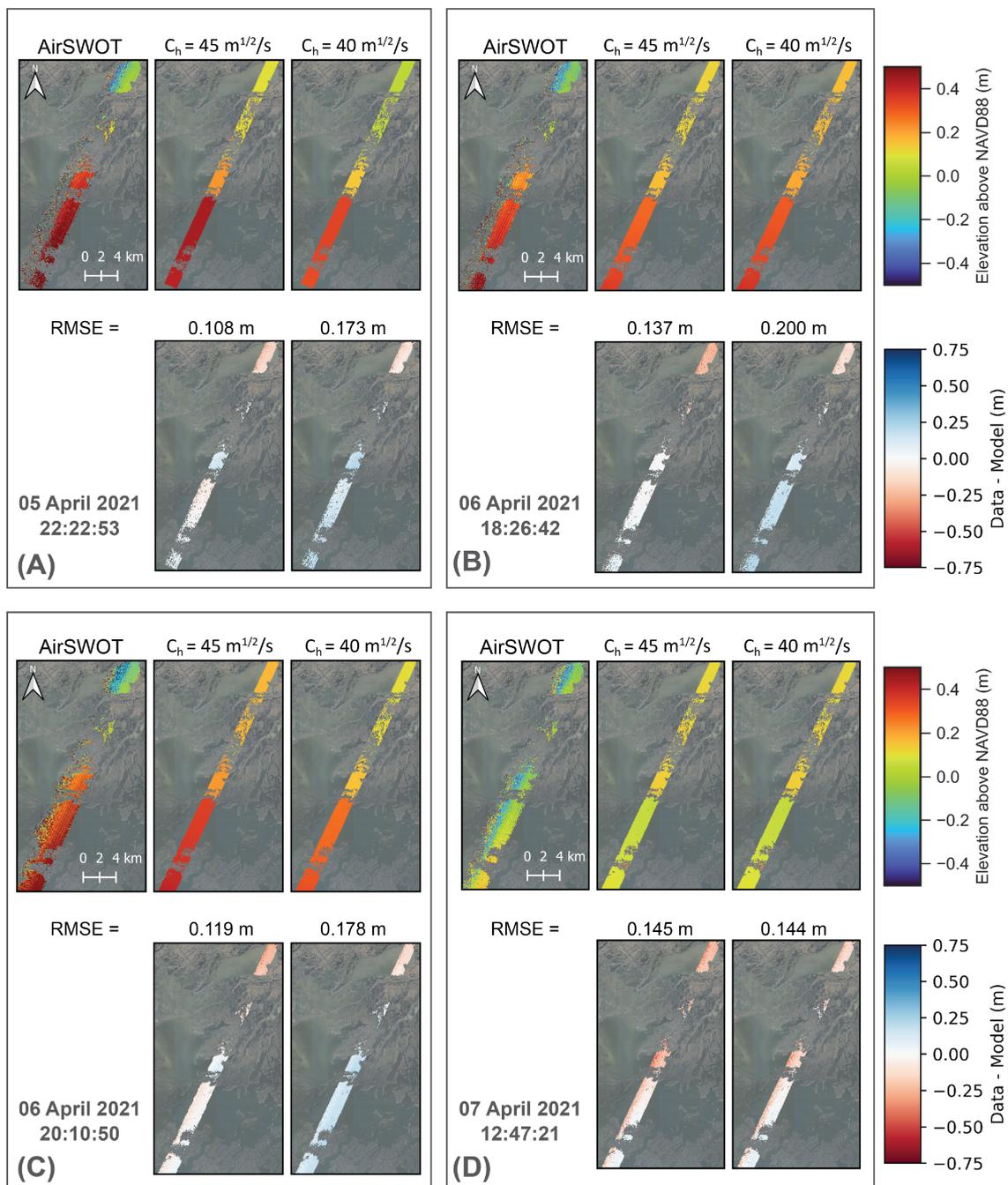
Figure 4. Comparison between measured water levels by AirSWOT and modelled water levels within the large scale Terrebonne model. In each of the four panels on the top row the measured and modelled water levels are shown (with C_h=45 m$^{1/2}$s^{-1}). On the bottom row the difference between AirSWOT and the model results are displayed with the overall RMSE. In each panel the date and time (GMT) of the acquisition is reported.
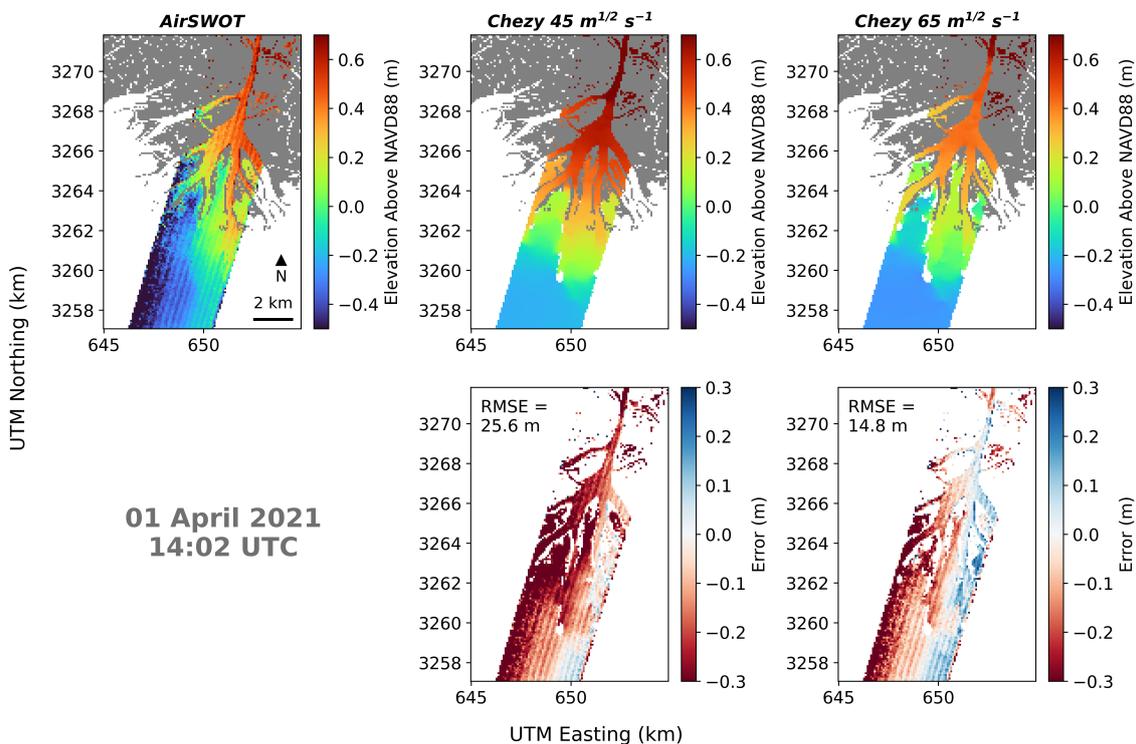
Figure 5. Comparison between measured water levels by AirSWOT and modelled water levels in Atchafalaya Bay (with focus on the Wax Lake Delta). From left to right are presented AirSWOT elevation, modelled elevation with $C_h = 45$ m$^{1/2}$s^{-1} and modelled elevation with $C_h = 65$ m$^{1/2}$s^{-1}.

3.2 Coupling with UAVSAR

Data of water-level changes measured during the 12 April 2021 UAVSAR flight were used to correct marsh topography. The campaign took place between t_1=19:29 and t_2= 22:59 (UTC time). The data collected in this temporal window offer a syn-

250 optic view of water-level change across the marsh landscape during falling tides. Since water level change is computed as the difference between the measurements at t_2 and t_1, the negative values in Figure 6d confirms that the waters on the marsh are receding. Results from the first run (Figure 6e) shows the tendency of the model to overestimate the water level change in the bottom area, indicating an error in the marsh elevation derived from LiDAR data. The opposite is verified in the northern area, where waters are found to recede too slowly and consequently underestimate the water level change. Thus, the original topog-

255 raphy (Figure 6a) was modified with the described step-wise approach, and after four iterations the new topography (Figure 6b) increased model performance (Figure 6b), with RMSE decreasing from 4.9 to 3.9 cm. The topography modifications (Figure 6c) well reproduce water level changes (Figure 6f), particularly in the critical areas previously highlighted.
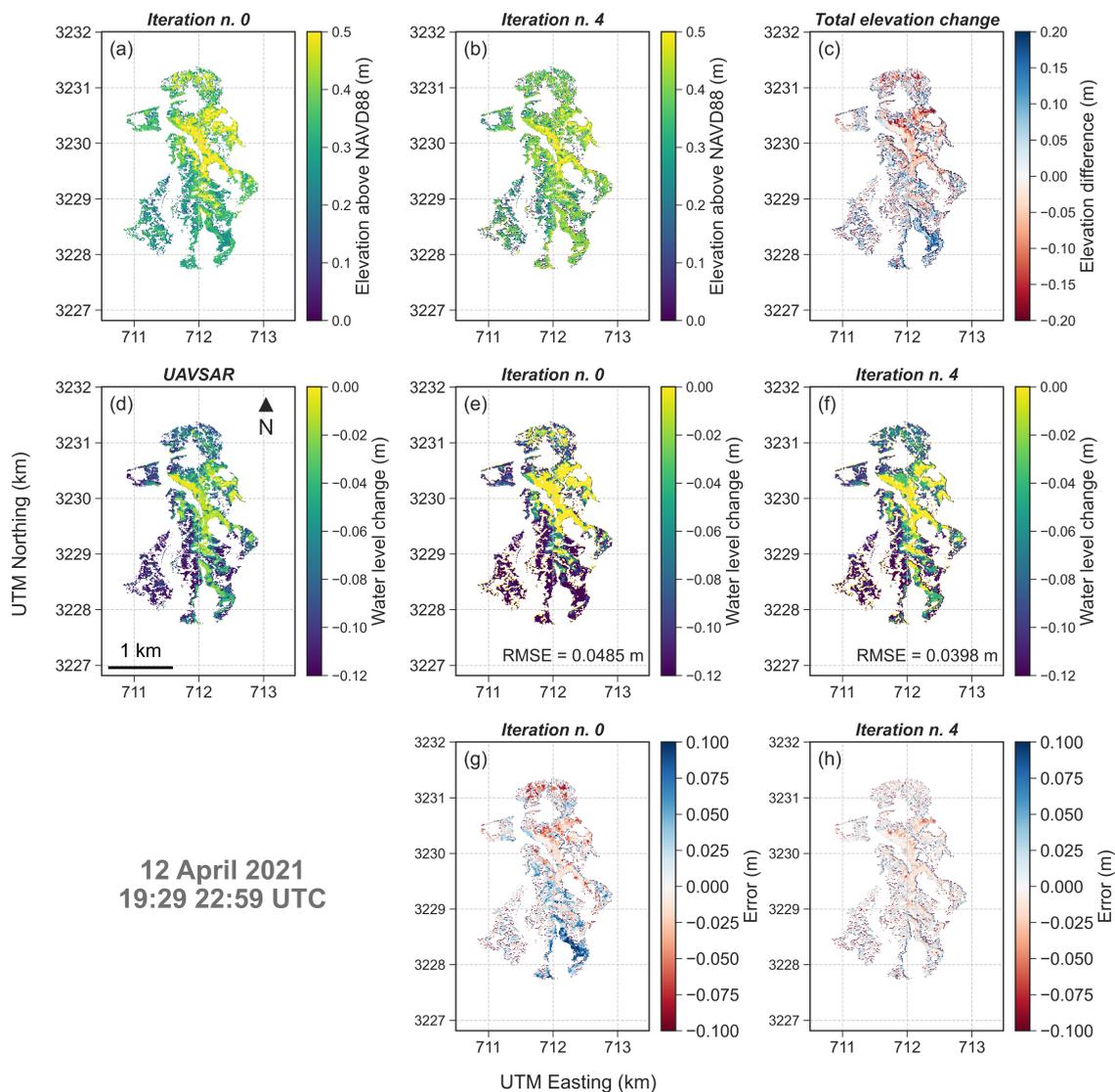
Figure 6. Comparison between (a) initial marsh topography and (b) marsh topography after four iterations of the correction method. Subplot (c) shows the total implemented changes in bed elevation. Elevation data are given with respect to NAVD88. Comparison between (d) water-level changes in vegetated areas measured by UAVSAR during the April 12 2021 UAVSAR flight between 19:29 and 22:59 (UTC time), and water-level changes obtained via numerical modelling by using: (e) the initial marsh topography, and (f) the topography after four iterations. Subplots (g) and (h) show the model error at first and fourth iteration respectively.

3.3 Coupling with AVIRIS-NG

First, for the Terrebonne model, the acquisition taken on 05 April 2021 at 19:57:00 GMT (Figure 7) is considered. The majority
260 of area within the line crosses the open coastal area and Caillou Lake from south-west to north-east. Results show that sediment
concentrations tend to decrease as the critical shear stress increases (Figure 7A). For $\tau_{cr,e}$ = 0.05 Pa, the models tends to
overestimate the sediment concentrations. The best agreement (lowest RMSE) occurs at value 0.1 Pa. For $\tau_{cr,e}$ = 0.125 and
0.15 Pa, the error increases again with an underestimation of sediment concentration. Figure 7B shows the effect of the settling
velocity. When w_s = 0.1 mm/s the sediment concentration is grossly overestimated. With higher values of settling velocity, the
265 comparison improves, until it reaches the lowest RMSE of 34.79 mg/L for w_s = 0.25 mm/s. For higher values, the agreement
declines, and the model tends to underestimate sediment concentrations. The flight line also crosses a meander of a large
channel (center-right position). Here, the model tends always to overestimate sediment concentration and the error decreases
as critical shear stress and settling velocity increases. Overall, the model better performs in the more open sections of the
flight line, while at the extremities, performance declines. Overall, the best combination that provides the best comparison with
270 measurements as a critical shear stress of 0.1 Pa and a sediment settling velocity of 0.25 mm/s.

For the Wax Lake model, the acquisition taken on 02 April 2021 at 19:59:22 GMT is considered. It is observed that a lower
critical shear stress generates higher sediment concentrations (Figure 8), consistent with the Terrebonne model. In particular,
the best comparison is given for $\tau_{cr,1}$ = 0.03 Pa (clay) and $\tau_{cr,2}$ = 0.1 Pa (silt), where the comparison between model and
observation gives a RMSE of 35.88 mg/L. In this case, results improve when waves are included in the simulation. This is
275 evident in the area near the shallow shoals near the delta, suggesting that wave resuspension must be included despite the river-
dominated system. In the other two cases the model tend to underestimate ($\tau_{cr,1}$ = 0.1 Pa and $\tau_{cr,2}$ = 0.2 Pa) and overestimate
($\tau_{cr,1}$ = 0.025 Pa and $\tau_{cr,2}$ = 0.05 Pa) sediment concentrations.

4 Discussion

The combination of AirSWOT, UAVSAR, and AVIRIS-NG enables calibration and evaluation of different parameters of the
280 numerical model at spatial scales that in-situ point measurements cannot capture. AirSWOT and UAVSAR data can greatly
improve hydrodynamic models. In particular their combination enables evaluation of the goodness of water fluxes in bays and
tidal channels, and on the marsh platform. AVIRIS-NG-derived sediment concentration enable evaluation of the models' ability
to reproduce sediment resuspension and transport.

4.1 AirSWOT

285 The comparison between hydrodynamic model and remote sensing imagery shows that the model is able to reproduce the
water levels in the lower half of the flight line. The calibrated value of 45 $\mathrm{m}^{1/2}\mathrm{s}^{-1}$ for the Chezy coefficient is comparable
to Manning values for the area. If we consider an average modelled water depth of 1.34 m during the AirSWOT acquisitions
and use the water depth as an approximation for hydraulic radius, we can estimate the correspondent Manning coefficient n =
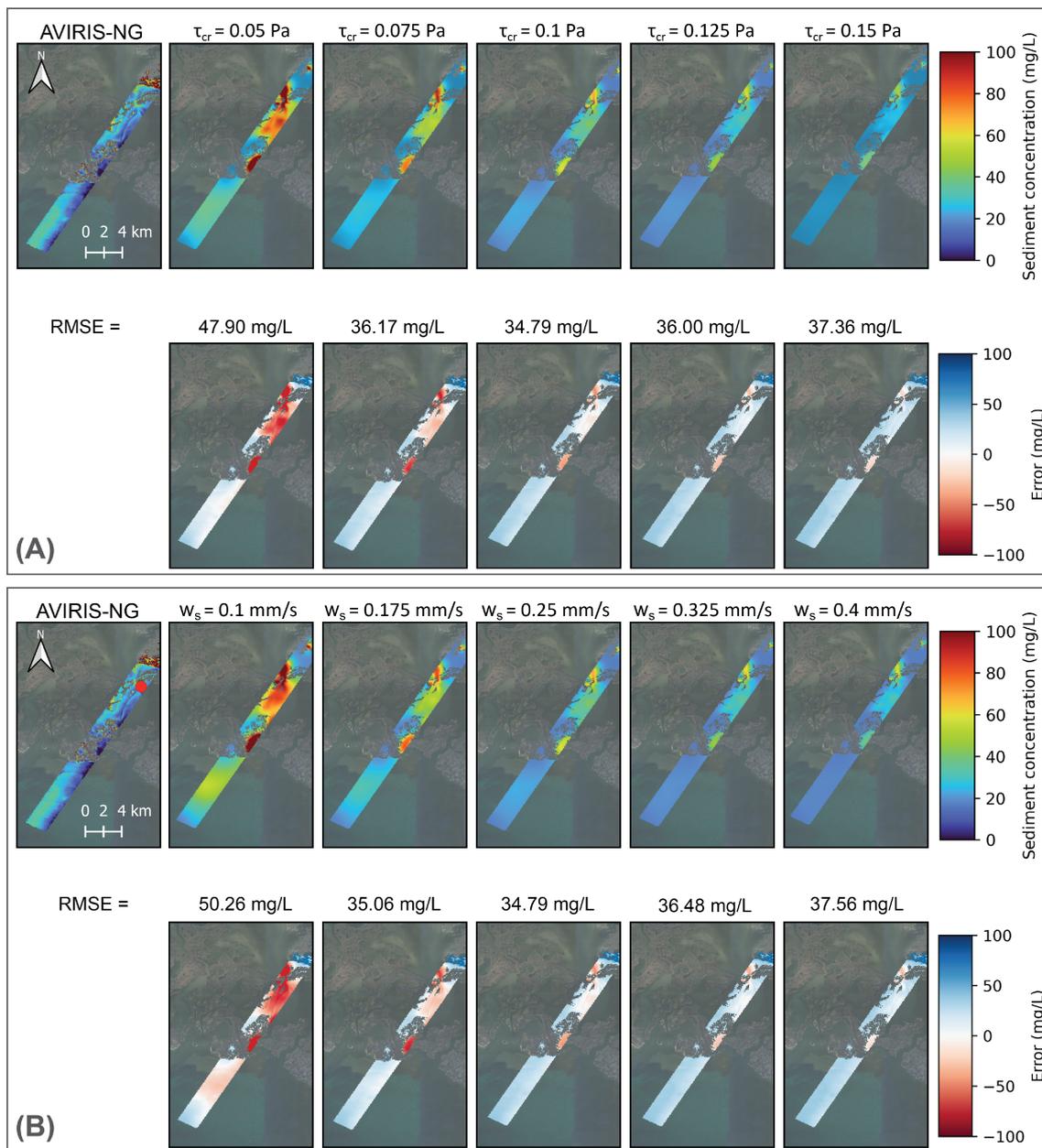
Figure 7. Comparison between AVIRIS-NG and the modelled sediment concentration. In Panel A, the settling velocity is fixed at 0.25 mm/s and the critical shear stress is changed, while in Panel B, the latter is fixed at 0.1 Pa and the settling velocity changed. In Panel B AVIRIS-NG map, the red dot locates the position of the in-situ TSS sample. For each panel the first map on the top row shows the sediment concentration derived from AVIRIS-NG, while the next five maps show the modelled sediment concentration for each case of critical shear stress and settling velocity. The bottom rows show the error between measurements and model. At the top of each error map the RMSE is indicated. The sediment concentration colorbar is fixed between the minimum and maximum value of the measured sediment concentration, while the error colorbar is fixed between the overall minimum and maximum computed error.
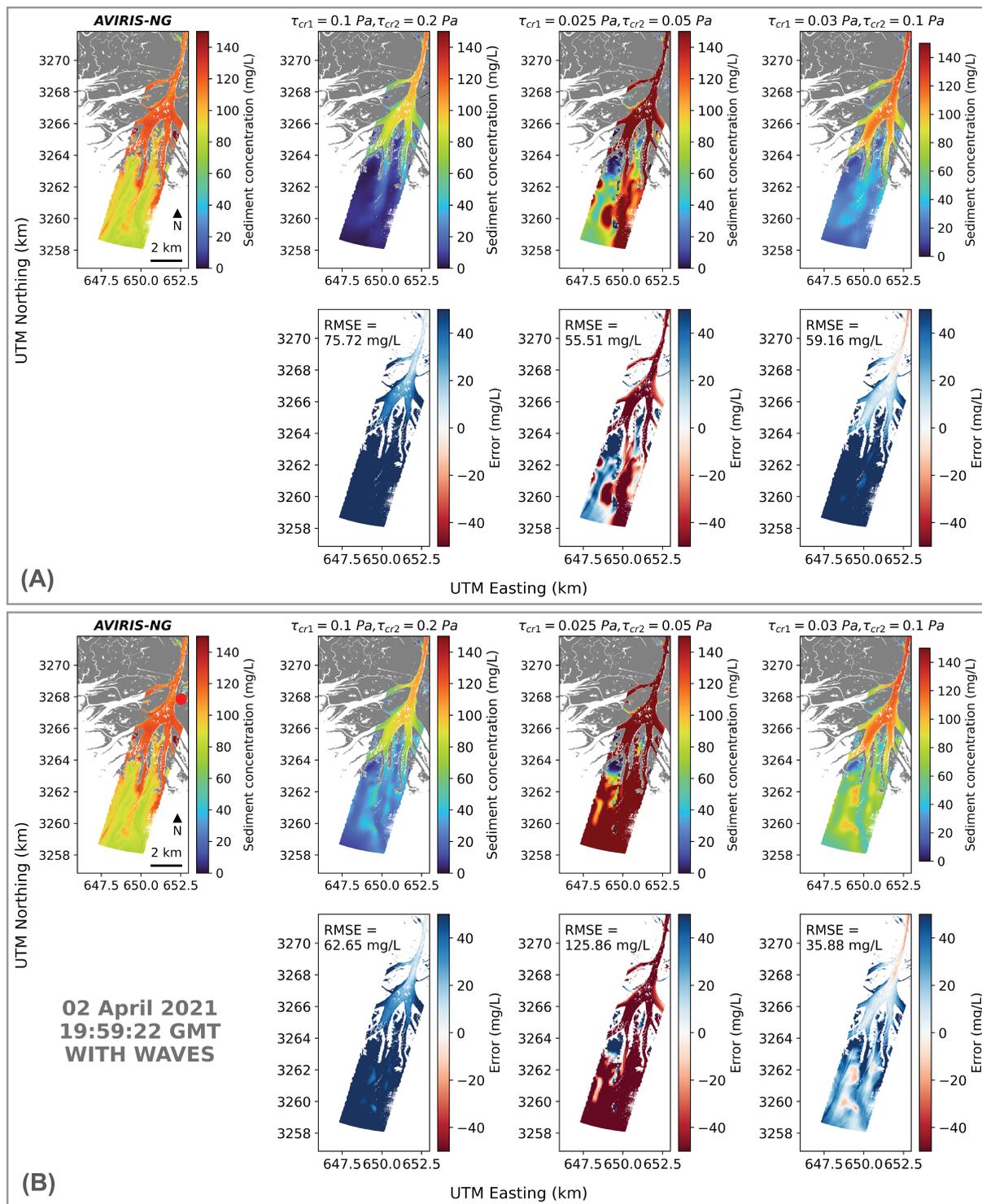
Figure 8. Comparison between AVIRIS-NG and the modelled sediment concentration in Wax Lake Delta. Scenarios show model results with different critical shear stresses for clay ($\tau_{cr,1}$) and silt ($\tau_{cr,2}$). Panel A reports results without waves, while Panel B results with waves.

$H^{1/6}C_h^{-1}$ (Limerinos, 1970). The equation yields n = 0.0233 $m^{1/3}s^{-1}$ which is within the range of values suggested by the
290 1992 NLCD and LA-GAP classification (Bunya et al., 2010).

In the northern areas of the large-scale Terrebonne Bay model, water levels tend to be regularly underestimated. AirSWOT
data highlight areas where model performance needs to be addressed. Errors can be related to uncalibrated bed friction coeffi-
cients. The model underestimates the water levels by 0.3 m on average, which represents a significant error since the average
tidal range is around 0.4 m (Georgiou et al., 2005). The issue could be addressed by increasing the Chezy coefficient, however
295 for such high discrepancy, it is likely to yield unrealistic values. In this case, there is a hydraulic connectivity problem, namely,
the model is not able to fully propagate the tides in the upper areas. The limitation lies in the coarse resolution of the mesh
(90x90 m), which cannot capture the intricate network of narrow channels that connects the upper and lower portions of the
domain. One way to address the issue is to carve and enlarge the channels until there is a satisfactory match between the remote
sensing data and the model (Zhang et al., 2022b).

300 In the Atchafalaya model, similar errors are observed to those described for Terrebonne. Water elevations in areas located
in the wetlands north of Wax Lake Delta tend to be overestimated. The reason can be similarly explained as in the Terrebonne
model, in that the low spatial resolution that does not correctly represent the narrow channels. However, the model well
replicated the water levels in the delta due to the wide cross section of the main distributaries (between 200-500 m).

It is also worth noting that before calibration with the remote sensing imagery, the correct boundary conditions must be
305 imposed. As mentioned previously, the boundary condition in the large-scale model is the water level signal from the Gulf of
Mexico, which was indirectly inferred from a USGS water level gauge located along the coast. Although it was not used here
for this purpose, AirSWOT can also be used to verify discharge boundary conditions in models where a riverine discharge is
imposed (Zhang et al., 2022a).

The validation of the water levels across the domain using in-situ measurements further confirms the goodness of the cal-
310 ibrated friction coefficient. Despite the lack of spatial information, timeseries can fill the temporal gap of the remote sensing
imagery. This highlights that a combination of both types of data is a powerful tool for a holistic calibration and validation of
numerical models.

4.2 UAVSAR

The difference between observed and modelled changes in water level over a fixed period of time were employed to correct
315 marsh topography. If such difference is large, more flow conveyance is needed to increase water level changes, and vice versa.
This can be done by modifying either the marsh elevation or the drag coefficient or both. As suggested by Zhang et al. (2022a),
friction plays a marginal role in affecting water levels on marsh platforms. As such, it was decided to only change marsh
elevation to match modelled water-level variations with those derived via UAVSAR.

The ability of a model to correctly simulate water fluxes is tightly dependent on having accurate and precise marsh topogra-
320 phy. This is especially true in locations such as coastal Louisiana where tidal ranges are small. Here, even a small topographic
change can lead to notable variations in the flooding period. Bathymetric data from LiDAR may present a positive bias in
vegetated areas due to the inability of laser pulses to penetrate dense thick vegetation (Rosso et al., 2006). Furthermore, such

bias is spatially variable and depends on vegetation characteristics (Medeiros et al., 2015). UAVSAR data can fill this gap. A simple comparison between model results and remote sensing data allowed precise identifications of critical parts of the do-

325 main and improvement of water fluxes on the marsh. The adjustment of the marsh elevation could be also carried out by adding or subtracting a constant value. However, UAVSAR allows to adjust the elevation at each point based on local hydrodynamics since it provides information, unraveling the effect of micro-topography on water flow.

Starting from the initial topography, in each iteration model performance the RMSE decreases until the minimum value of 3.9 cm is reached at the fourth iteration. After this iterations, the error in the subsequent ones increases. It is important

330 to highlight that this methodology is empirical and might have some theoretical issues. For instance, by modifying the bed elevation at some location of a marsh, water levels will change in the surrounding areas. Thus, this iterative procedure might introduce errors in areas where the topography is correct. This is what happens after the fourth iteration, where the procedure begins to over-correct the topography and introduces errors that result in worst performance.

Another drawback of this approach is that the bathymetric correction is based on the water-level changes detected by the radar

335 instrument during the UAVSAR flight on April 12 2021 between 19:29 to 22:59 (UTC time). Such changes are representative over a limited time length and are related to the temporal window in which the UAVSAR campaign took place. Although the solution was improved, the choice of a different acquisition might yield a different final marsh topography.

4.3 AVIRIS-NG

The use of AVIRIS-NG is possible after the calibration and validation of the hydrodynamic model, since sediment concentration

340 depends on the properties of sediment particles and hydrodynamic forcing. For the large-scale Terrebonne model, the calibrated critical shear stress and settling velocity are comparable with those of previous studies of the Terrebonne area (e.g., Liu et al. (2018)). Along the flight line, the lower portion in the coastal waters of the Gulf of Mexico and the Caillou Lake portion in the middle provide the best match with the imagery, despite the fact that the modelled concentration tends to be more homogeneous. Overall, considering the relatively low RMSE compared to the full range of sediment concentration, it is concluded that the

345 model is able to capture the resuspension. The model is also able to reproduce the sediment plume entering Caillou Lake with the tendency to overestimate the concentration. Concurrently to the AVIRIS-NG acquisition, an in-situ sample was collected (see red dot in Figure 7B) with TSS concentration of 48.7 mg/L. At this location, the model with the best set of parameters (w_s = 0.25 mm/s, $\tau_{cr,e}$ = 0.1 Pa) underestimates the concentration by computing 21.43 mg/L. The model with one of worst set of parameters (w_s = 0.25 mm/s, $\tau_{cr,e}$ = 0.05 Pa) returns a concentration of 52.19 mg/L, a values much closer to the measurement.

350 A similar situation can be found for the Atchafalaya model, where a TSS sample was collected along a secondary channel (see red dot in Figure 8B) for which 112.2 mg/L was measured. Here, the model with the best set of parameters ($\tau_{cr,1}$ = 0.03 Pa, $\tau_{cr,2}$ = 0.1 Pa) underestimates the concentration at 27.9 mg/L. However, the model with the worst set of parameters ($\tau_{cr,1}$ = 0.025 Pa, $\tau_{cr,2}$ = 0.05 Pa) returns a value of 100.96 mg/L. Despite being comparisons with single points, this shows that measurements located in fixed locations might be non representative and potentially lead to incorrect calibration parameters.

355 Especially in coastal areas, both settling velocity and bed shear strength of cohesive particles are highly uncertain and difficult to predict due to the flocculation, in which particles aggregate forming flocs, which have higher settling velocities compared to
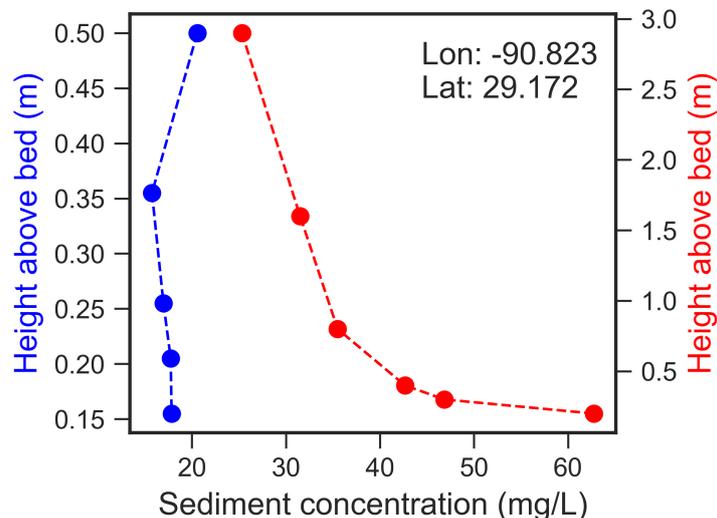
Figure 9. Vertical profiles of sediment concentration captured on the same location in two different dates. The samples were collected near CRMS sites 421 (red dot in Figure 1b) in the left channel of the Terrebonne small scale model. The blue profile on the left was collected on 17 August 2021 when the water depth was 0.55 m. The red profile was collected on 19 August 2021 when the water depth was 3 m.

the single particles they are made of. In this context, maps of TSS derived from AVIRIS-NG offers a synoptic view, allowing a more spatially informed way to calibrate these uncertain parameters.

In the Terrebonne large scale model there are also discrepancies at the upper areas and the channel meander in the center-right
360   areas of the flight line, where the model tends to overestimate sediment concentrations. These errors might be related to some the bathymetric modification. To allow a correct tidal propagation, channels were dredged and enlarged, which might generated different flow velocity compared to the real ones. Errors can also be attributable to some assumptions that are inherent to the developed model. Although Delft3D has tri-dimensional capabilities, it was opted for a vertically averaged 2D model to avoid high computational costs and because of the numerical instability of 3D grids when wetting and drying dynamics in tidal flats
365   and salt marshes are included. Moreover, tri-dimensional models do not provide a substantial improvement of predictability in water levels with respect to bi-dimensional models (Bates, 2022).

It is fundamental to consider that AVIRIS-NG measures TSS concentration at the water surface. Since the models are depth-averaged, a well-mixed column is implicitly assumed, which is a condition that might not always be true. For example, Figure 9 shows two examples of suspended sediment concentration (SSC) measured along the water column at the same location, but
370   on different dates (Nghiem et al., 2022).

Data in Figure 9 show that a depth averaged sediment concentration is not always representative. Along rivers, sediment concentration has been typically observed to increase from the surface to the bed (Lamb et al., 2020). The well-mixed condition can be valid in sheltered areas. In these locations, vertical heterogeneity is promoted by density gradients and low energy conditions during low wind speed conditions (Kjerfve and Magill, 1989). Another possible source of error due to the bi-

375 dimensional nature of the model is the absence of secondary flows and 3D flow structures that might arise at the boundary between channels and marsh platform (Proust and Nikora, 2020).

The AVIRIS-NG data suggest further evaluations. The comparison between the wave and no-wave cases (Figure 8) shows that the inclusion of the wave-induced resuspension is fundamental to better capture SSC in the delta areas. This result is consistent with previous research that highlighted the important role of waves in the development of river deltas and the redis-
380 tribution of sediment along the coastal inner shelf (Shi et al., 1997; Walker and Hammack, 2000; Corbett et al., 2007; Carniello et al., 2014). As final note, it is worth to mention that maps of TSS from AVIRIS-NG can also be leveraged independently from the numerical model. For instance, TSS maps in the Wax Lake Delta reveal distinctive patterns called streaklines (Kundu et al., 2015) (see Figure 2c), that can be used to derive deposition/erosion patterns and flow velocity without the support of numerical models (Salter et al., 2022; Donatelli et al., 2023).

385 ## 5 Conclusions

This study shows the potential of calibrating different Delft3D numerical models using remote sensing imagery instead of traditional sparse field data. Images from two SAR sensors and one spectrometer sensor used during the recent NASA Delta-X airborne mission were adopted. UAVSAR measured water level change on the marsh platform, while AirSWOT derived water elevations in bays, lakes, channels, and AVIRIS-NG measured sediment concentrations.

390 AirSWOT was used to calibrate the bottom friction coefficient in Terrebonne and Atchafalaya Basins, UAVSAR data to correct bathymetric errors and improve wetland flooding, and TSS maps derived from AVIRIS-NG allowed to calibrate sediment transport parameters. The use of spatially extended remote sensing imagery enabled to quickly evaluate areas where models performed better and provided calibrated parameters that are consistent with previous literature values. Remote sensing data yield spatial information that point observations cannot capture. In the case of highly uncertain parameters, having a calibra-
395 tion based entirely on fixed location measurements can lead to wrong values, while imagery from remote sensing can provide more spatially coherent values. At the same time, some limitations and considerations need to be accounted for when coupling imagery with a numerical model.

Finally, the use of water level time series at different locations for the validation informed the temporal performance of the models. Given the limited number of flyovers, these data allow to verify the accuracy of the calibration and test whether the
400 model reproduces coherent water elevations over a wider time window in specific points of the domain.

The array of available remote sensing data will grow in the near future. This study showed that a new generation of numerical models will be developed by leveraging the spatial information provided by remote sensors.

Data availability. All Delta-X products and data used in this study are deposited at the correspondent ORNL-DAAC repository (https://daac.ornl.gov/daacdata/deltax/). Water level data from the Coastwide Reference Monitoring System (CRMS) used for the large scale
405 Terrebonne model validation and small scale Terrebonne model boundary conditions are publicly available via the CPRA website (https:

//cims.coastal.louisiana.gov/monitoring-data/). Water levels data from the USGS station 073813498 used as boundary conditions in the large scale Terrebonne model are available via the USGS website (https://waterdata.usgs.gov/monitoring-location/073813498/#parameterCode=00065&period=P7D). Water discharge and sediment concentration data for the Atchafalaya model from the USGS stations 07381590 and 07381600 are available via the USGS website (https://waterdata.usgs.gov/monitoring-location/07381590/#parameterCode=00065&period=

410 P7D) and (https://waterdata.usgs.gov/monitoring-location/07381600/#parameterCode=00065&period=P7D) respectively. Water level data from the Eugene Island NOAA station used as oceanic boundary condition in the Atchafalaya model are available via the NOAA website (https://tidesandcurrents.noaa.gov/stationhome.html?id=8764314).

Author contributions. LC, CD, XZ performed the simulations and interpreted the results. SF supervised the project. LC wrote the manuscript with contributions from all co-authors.

415 *Competing interests.* The authors declare that there is no conflict of interest regarding the publication of this article.

Acknowledgements. This research was funded by the NASA Delta-X project (the Science Mission Directorate's Earth Science Division through the Earth Venture Suborbital-3 Program NNH17ZDA001N-EVS3). LC was supported by the Future Investigators in NASA Earth and Space Science and Technology (FINNEST) award number 80NSSC21K1612. SF was also supported by the Virginia Coast Reserve Long-Term Ecological Research Program (National Science Foundation DEB-1832221) and the Plum Island Ecosystems Long-Term Eco-

420 logical Research Program (National Science Foundation OCE-2224608). This work was carried out in part at the Jet Propulsion Laboratory, California Institute of Technology, under a contract with the National Aeronautics and Space Administration.

References

Allison, M. A., Kineke, G. C., Gordon, E. S., and Goni, M. A.: Development and reworking of a seasonal flood deposit on the inner continental shelf off the Atchafalaya River, Continental Shelf Research, 20, 2267–2294, https://doi.org/10.1016/S0278-4343(00)00070-4, 2000.

425 Balogun, A.-L., Yekeen, S. T., Pradhan, B., and Althuwaynee, O. F.: Spatio-temporal analysis of oil spill impact and recovery pattern of coastal vegetation and wetland using multispectral satellite landsat 8-OLI imagery and machine learning models, Remote Sensing, 12, 1225, https://doi.org/10.3390/rs12071225, 2020.

Bates, P. D.: Flood inundation prediction, Annual Review of Fluid Mechanics, 54, 287–315, https://doi.org/10.1146/annurev-fluid-030121-113138, 2022.

430 Bevington, A. E. and Twilley, R. R.: Island edge morphodynamics along a chronosequence in a prograding deltaic floodplain wetland, Journal of Coastal Research, 34, 806–817, https://doi.org/10.2112/JCOASTRES-D-17-00074.1, 2018.

Booij, N. and Holthuijsen, L. H.: Propagation of ocean waves in discrete spectral wave models, Journal of Computational Physics, 68, 307–326, https://doi.org/10.1016/0021-9991(87)90060-X, 1987.

Bue, B. D., Thompson, D. R., Eastwood, M., Green, R. O., Gao, B.-C., Keymeulen, D., Sarture, C. M., Mazer, A. S., and Luong, H. H.:
435 Real-time atmospheric correction of AVIRIS-NG imagery, IEEE Transactions on Geoscience and Remote Sensing, 53, 6419–6428, https://doi.org/10.1109/TGRS.2015.2439215, 2015.

Bunya, S., Dietrich, J. C., Westerink, J., Ebersole, B., Smith, J., Atkinson, J., Jensen, R., Resio, D., Luettich, R., Dawson, C., et al.: A high-resolution coupled riverine flow, tide, wind, wind wave, and storm surge model for southern Louisiana and Mississippi. Part I: Model development and validation, Monthly weather review, 138, 345–377, https://doi.org/10.1175/2009MWR2906.1, 2010.

440 Cahoon, D. R., Hensel, P. F., Spencer, T., Reed, D. J., McKee, K. L., and Saintilan, N.: Coastal wetland vulnerability to relative sea-level rise: wetland elevation trends and process controls, Wetlands and natural resource management, pp. 271–292, https://doi.org/10.1007/978-3-540-33187-2_12, 2006.

Cardoso, G. F., Souza, C., and Souza-Filho, P. W. M.: Using spectral analysis of Landsat-5 TM images to map coastal wetlands in the Amazon River mouth, Brazil, Wetlands ecology and management, 22, 79–92, https://doi.org/10.1007/s11273-013-9324-4, 2014.

445 Carniello, L., Silvestri, S., Marani, M., D'Alpaos, A., Volpe, V., and Defina, A.: Sediment dynamics in shallow tidal basins: In situ observations, satellite retrievals, and numerical modeling in the Venice Lagoon, Journal of Geophysical Research: Earth Surface, 119, 802–815, https://doi.org/10.1002/2013JF003015, 2014.

Castagno, K. A., Jiménez-Robles, A. M., Donnelly, J. P., Wiberg, P. L., Fenster, M. S., and Fagherazzi, S.: Intense storms increase the stability of tidal bays, Geophysical Research Letters, 45, 5491–5500, https://doi.org/10.1029/2018GL078208, 2018.

450 Chen, C., Ma, Y., Ren, G., and Wang, J.: Aboveground biomass of salt-marsh vegetation in coastal wetlands: Sample expansion of in situ hyperspectral and Sentinel-2 data using a generative adversarial network, Remote Sensing of Environment, 270, 112 885, https://doi.org/10.1016/j.rse.2021.112885, 2022.

Corbett, D. R., Dail, M., and McKee, B.: High-frequency time-series of the dynamic sedimentation processes on the western shelf of the Mississippi River Delta, Continental Shelf Research, 27, 1600–1615, https://doi.org/10.1016/j.csr.2007.01.025, 2007.

455 Cortese, L. and Fagherazzi, S.: Fetch and distance from the bay control accretion and erosion patterns in Terrebonne marshes (Louisiana, USA), Earth Surface Processes and Landforms, 47, 1455–1465, https://doi.org/10.1002/esp.5327, 2022.

Couvillion, B. R., Beck, H., Schoolmaster, D., and Fischer, M.: Land area change in coastal Louisiana (1932 to 2016), Tech. rep., US Geological Survey, https://doi.org/10.3133/sim3381, 2017.

Defne, Z. and Ganju, N. K.: Quantifying the residence time and flushing characteristics of a shallow, back-barrier estuary: Application of hydrodynamic and particle tracking models, Estuaries and Coasts, 38, 1719–1734, https://doi.org/10.1007/s12237-014-9885-3, 2015.

Denbina, M., Simard, M., Rodriguez, E., Wu, X., Chen, A., and Pavelsky, T.: Mapping water surface elevation and slope in the mississippi river delta using the AirSWOT Ka-Band interferometric synthetic aperture radar, Remote Sensing, 11, 2739, https://doi.org/10.3390/rs11232739, 2019.

Denbina, M., Simard, M., Pavelsky, T., Christensen, A., Liu, K., and Lyon, C.: Pre-Delta-X: Channel Bathymetry of the Atchafalaya Basin, LA, USA, 2016, ORNL DAAC, https://doi.org/10.3334/ORNLDAAC/1807, 2020.

Denbina, M., Simard, M., and Rodriguez, E.: Delta-X: AirSWOT L2 Geocoded Water Surface Elevation, MRD, Louisiana, 2021, Version 2. ORNL DAAC, Oak Ridge, Tennessee, USA, https://doi.org/10.3334/ORNLDAAC/2128, 2022.

Dietrich, J., Westerink, J., Kennedy, A., Smith, J., Jensen, R., Zijlema, M., Holthuijsen, L., Dawson, C., Luettich, R., Powell, M., et al.: Hurricane Gustav (2008) waves and storm surge: hindcast, synoptic analysis, and validation in Southern Louisiana, Monthly Weather Review, 139, 2488–2522, https://doi.org/10.1175/2011MWR3611.1, 2011.

Donatelli, C., Passalacqua, P., Wright, K., Salter, G., Lamb, M. P., Jensen, D., and Fagherazzi, S.: Quantifying flow velocities in river deltas via remotely sensed suspended sediment concentration, Geophysical Research Letters, 50, e2022GL101 392, https://doi.org/10.1029/2022GL101392, 2023.

Dorji, P. and Fearns, P.: A quantitative comparison of total suspended sediment algorithms: A case study of the last decade for MODIS and landsat-based sensors, Remote Sensing, 8, 810, https://doi.org/10.3390/rs8100810, 2016.

Fagherazzi, S., Mariotti, G., Leonardi, N., Canestrelli, A., Nardin, W., and Kearney, W. S.: Salt marsh dynamics in a period of accelerated sea level rise, Journal of Geophysical Research: Earth Surface, 125, e2019JF005 200, https://doi.org/10.1029/2019JF005200, 2020.

Farber, S.: The value of coastal wetlands for protection of property against hurricane wind damage, Journal of Environmental Economics and Management, 14, 143–151, https://doi.org/10.1016/0095-0696(87)90012-X, 1987.

Fichot, C. and Harringmeyer, J.: Delta-X: AVIRIS-NG L3-derived Water Quality, TSS, and Turbidity, MRD, LA 2021, V2, ORNL DAAC, https://doi.org/10.3334/ORNLDAAC/2112, 2022.

Fichot, C., Ghosh, N., Harringmeyer, J., and Weiser, M.: Delta-X: Total Suspended Solids Concentration across MRD, LA, USA, 2021, Version 2, ORNL DAAC, https://doi.org/10.3334/ORNLDAAC/2075, 2022.

Fichot, C. G., Downing, B. D., Bergamaschi, B. A., Windham-Myers, L., Marvin-DiPasquale, M., Thompson, D. R., and Gierach, M. M.: High-resolution remote sensing of water quality in the San Francisco Bay–Delta Estuary, Environmental Science & Technology, 50, 573–583, https://doi.org/10.1021/acs.est.5b03518, 2016.

Galbraith, H., Jones, R., Park, R., Clough, J., Herrod-Julius, S., Harrington, B., and Page, G.: Global climate change and sea level rise: potential losses of intertidal habitat for shorebirds, Waterbirds, 25, 173–183, https://doi.org/10.1675/1524-4695(2002)025[0173:GCCASL]2.0.CO;2, 2002.

Ganju, N. K., Defne, Z., Kirwan, M. L., Fagherazzi, S., D'Alpaos, A., and Carniello, L.: Spatially integrative metrics reveal hidden vulnerability of microtidal salt marshes, Nature communications, 8, 14 156, https://doi.org/10.1038/ncomms14156, 2017.

Gao, B.-C., Heidebrecht, K. B., and Goetz, A. F.: Derivation of scaled surface reflectances from AVIRIS data, Remote sensing of Environment, 44, 165–178, https://doi.org/10.1016/0034-4257(93)90014-O, 1993.

Georgiou, I. Y., FitzGerald, D. M., and Stone, G. W.: The impact of physical processes along the Louisiana coast, Journal of Coastal Research, pp. 72–89, http://www.jstor.org/stable/25737050, 2005.

Ghosh, S., Mishra, D. R., and Gitelson, A. A.: Long-term monitoring of biophysical characteristics of tidal wetlands in the northern Gulf of Mexico—A methodological approach using MODIS, Remote Sensing of Environment, 173, 39–58, https://doi.org/10.1016/j.rse.2015.11.015, 2016.

Goldstein, R. M. and Zebker, H.: Interferometric radar measurement of ocean surface currents, Nature, 328, 707–709, https://doi.org/10.1038/328707a0, 1987.

Guo, M., Li, J., Sheng, C., Xu, J., and Wu, L.: A review of wetland remote sensing, Sensors, 17, 777, https://doi.org/10.3390/s17040777, 2017.

Haddad, J., Lawler, S., and Ferreira, C. M.: Assessing the relevance of wetlands for storm surge protection: a coupled hydrodynamic and geospatial framework, Natural Hazards, 80, 839–861, https://doi.org/10.1007/s11069-015-2000-7, 2016.

Hamlin, L., Green, R., Mouroulis, P., Eastwood, M., Wilson, D., Dudik, M., and Paine, C.: Imaging spectrometer science measurements for terrestrial ecology: AVIRIS and new developments, in: 2011 Aerospace conference, pp. 1–7, IEEE, https://doi.org/10.1109/AERO.2011.5747395, 2011.

Henderson, F. M. and Lewis, A. J.: Radar detection of wetland ecosystems: a review, International journal of remote sensing, 29, 5809–5835, https://doi.org/10.1080/01431160801958405, 2008.

Holthuijsen, L., Booij, N., and Ris, R.: A spectral wave model for the coastal zone, in: Ocean wave measurement and analysis, pp. 630–641, ASCE, 1993.

Hong, S.-H. and Wdowinski, S.: Multitemporal Multitrack Monitoring of Wetland Water Levels in the Florida Everglades Using ALOS PALSAR Data With Interferometric Processing, IEEE Geoscience and Remote Sensing Letters, 11, 1355–1359, https://doi.org/10.1109/LGRS.2013.2293492, 2014.

Ill, E. W. R., Chappell, D. K., and Baldwin, D. G.: AVHRR lmagery used to identify hurricane damage in a forested wetland of Louisiana, Photogrammetric Engineering & Remote Sensing, 63, 293–297, http://pubs.er.usgs.gov/publication/70020165, 1997.

Jensen, D., Simard, M., Cavanaugh, K., Sheng, Y., Fichot, C. G., Pavelsky, T., and Twilley, R.: Improving the transferability of suspended solid estimation in wetland and deltaic waters with an empirical hyperspectral approach, Remote Sensing, 11, 1629, https://doi.org/10.3390/rs11131629, 2019.

Jensen, D., Cavanaugh, K. C., Simard, M., Christensen, A., Rovai, A., and Twilley, R.: Aboveground biomass distributions and vegetation composition changes in Louisiana's Wax Lake Delta, Estuarine, Coastal and Shelf Science, 250, 107 139, https://doi.org/https://doi.org/10.1016/j.ecss.2020.107139, 2021.

Jensen, D., Cavanaugh, K., Thompson, D., Fagherazzi, S., Cortese, L., and Simard, M.: Leveraging the historical Landsat catalog for a remote sensing model of wetland accretion in coastal Louisiana, Journal of Geophysical Research: Biogeosciences, 127, e2022JG006 794, https://doi.org/10.1029/2022JG006794, 2022.

Jones, C., Oliver-Cabrera, T., Simard, M., and Lou, Y.: Delta-X: UAVSAR L3 Water Level Changes, MRD, Louisiana, 2021, ORNL DAAC, https://doi.org/10.3334/ORNLDAAC/2058, 2022.

Kang, X., Yan, L., Zhang, X., Li, Y., Tian, D., Peng, C., Wu, H., Wang, J., and Zhong, L.: Modeling gross primary production of a typical coastal wetland in China using MODIS time series and CO_2 eddy flux tower data, Remote Sensing, 10, 708, https://doi.org/10.3390/rs10050708, 2018.

Kaplan, G. and Avdan, U.: Mapping and monitoring wetlands using Sentinel-2 satellite imagery, https://doi.org/10.5194/isprs-annals-IV-4-W4-271-2017, 2017.

Kim, J.-W., Lu, Z., Lee, H., Shum, C., Swarzenski, C. M., Doyle, T. W., and Baek, S.-H.: Integrated analysis of PALSAR/Radarsat-1 InSAR and ENVISAT altimeter data for mapping of absolute water level changes in Louisiana wetlands, Remote Sensing of Environment, 113, 2356–2365, https://doi.org/10.1016/j.rse.2009.06.014, 2009.

Kjerfve, B. and Magill, K. E.: Geographic and hydrodynamic characteristics of shallow coastal lagoons, Marine geology, 88, 187–199, https://doi.org/10.1016/0025-3227(89)90097-2, 1989.

Kundu, P. K., Cohen, I. M., and Dowling, D. R.: Fluid mechanics, Academic press, 2015.

Kwoun, O.-i. and Lu, Z.: Multi-temporal RADARSAT-1 and ERS backscattering signatures of coastal wetlands in southeastern Louisiana, Photogrammetric Engineering & Remote Sensing, 75, 607–617, https://doi.org/10.14358/PERS.75.5.607, 2009.

Lamb, M. P., de Leeuw, J., Fischer, W. W., Moodie, A. J., Venditti, J. G., Nittrouer, J. A., Haught, D., and Parker, G.: Mud in rivers transported as flocculated and suspended bed material, Nature Geoscience, 13, 566–570, https://doi.org/10.1038/s41561-020-0602-5, 2020.

Lesser, G., Roelvink, J., van Kester, J., and Stelling, G.: Development and validation of a three-dimensional morphological model, Coastal Engineering, 51, 883–915, https://doi.org/10.1016/j.coastaleng.2004.07.014, 2004.

Liao, T.-H., Simard, M., Denbina, M., and Lamb, M. P.: Monitoring water level change and seasonal vegetation change in the coastal wetlands of louisiana using L-band time-series, Remote Sensing, 12, 2351, https://doi.org/10.3390/rs12152351, 2020.

Limerinos, J. T.: Determination of the Manning coefficient from measured bed roughness in natural channels, vol. 1898, US Government Printing Office Washington, DC, https://doi.org/10.3133/wsp1898B, 1970.

Liu, K., Chen, Q., Hu, K., Xu, K., and Twilley, R. R.: Modeling hurricane-induced wetland-bay and bay-shelf sediment fluxes, Coastal Engineering, 135, 77–90, https://doi.org/10.1016/j.coastaleng.2017.12.014, 2018.

Lopes, C. L., Mendes, R., Caçador, I., and Dias, J. M.: Evaluation of long-term estuarine vegetation changes through Landsat imagery, Science of the Total Environment, 653, 512–522, https://doi.org/10.1016/j.scitotenv.2018.10.381, 2019.

Love, M. R., Caldwell, R. J., Carignan, K. S., and Eakins, B Wand Taylor, L. A.: Digital Elevation Model of Southern Louisiana: Procedures., Data Sources and Analysis, 22, 2010.

Lumbierres, M., Méndez, P. F., Bustamante, J., Soriguer, R., and Santamaría, L.: Modeling biomass production in seasonal wetlands using MODIS NDVI land surface phenology, Remote Sensing, 9, 392, https://doi.org/10.3390/rs9040392, 2017.

McClain, C. R. and Meister, G.: Mission Requirements for Future Ocean-Colour Sensors., https://doi.org/10.25607/OBP-104, 2012.

Medeiros, S., Hagen, S., Weishampel, J., and Angelo, J.: Adjusting lidar-derived digital terrain models in coastal marshes based on estimated aboveground biomass density, Remote Sensing, 7, 3507–3525, https://doi.org/10.3390/rs70403507, 2015.

Minello, T. J., Able, K. W., Weinstein, M. P., and Hays, C. G.: Salt marshes as nurseries for nekton: testing hypotheses on density, growth and survival through meta-analysis, Marine Ecology Progress Series, 246, 39–59, https://doi.org/10.3354/meps246039, 2003.

Möller, I., Kudella, M., Rupprecht, F., Spencer, T., Paul, M., Van Wesenbeeck, B. K., Wolters, G., Jensen, K., Bouma, T. J., Miranda-Lange, M., et al.: Wave attenuation over coastal salt marshes under storm surge conditions, Nature Geoscience, 7, 727–731, https://doi.org/10.1038/ngeo2251, 2014.

Muro, J., Canty, M., Conradsen, K., Hüttich, C., Nielsen, A. A., Skriver, H., Remy, F., Strauch, A., Thonfeld, F., and Menz, G.: Short-term change detection in wetlands using Sentinel-1 time series, Remote Sensing, 8, 795, https://doi.org/10.3390/rs8100795, 2016.

Nahlik, A. M. and Fennessy, M. S.: Carbon storage in US wetlands, Nature Communications, 7, 1–9, https://doi.org/10.1038/ncomms13835, 2016.

Nghiem, J., Salter, G., and Lamb, M.: Delta-X: Bed and Suspended Sediment Grain Size, Wax Lake Delta, LA, USA, 2021, ORNL DAAC, https://doi.org/10.3334/ORNLDAAC/2135, 2022.

Nicholls, R. J.: Coastal flooding and wetland loss in the 21st century: changes under the SRES climate and socio-economic scenarios, Global Environmental Change, 14, 69–86, https://doi.org/10.1016/j.gloenvcha.2003.10.007, 2004.

Oliver-Cabrera, T., Jones, C. E., Yunjun, Z., and Simard, M.: InSAR phase unwrapping error correction for rapid repeat measurements of water level change in wetlands, IEEE Transactions on Geoscience and Remote Sensing, 60, 1–15, https://doi.org/10.1109/TGRS.2021.3108751, 2021.

Parker, G. and Sequeiros, O.: Large scale river morphodynamics: Application to the Mississippi Delta, in: River Flow 2006: proceedings of the international conference on Fluvial Hydraulics, pp. 3–11, Taylor and Francis London, https://doi.org/10.1201/9781439833865.ch1, 2006.

Partheniades, E.: Erosion and deposition of cohesive soils, Journal of the Hydraulics Division, 91, 105–139, https://doi.org/10.1061/JYCEAJ.0001165, 1965.

Peter Sheng, Y., Paramygin, V. A., Rivera-Nieves, A. A., Zou, R., Fernald, S., Hall, T., and Jacob, K.: Coastal marshes provide valuable protection for coastal communities from storm-induced wave, flood, and structural loss in a changing climate, Scientific Reports, 12, 3051, https://doi.org/10.1038/s41598-022-06850-z, 2022.

Pflugmacher, D., Krankina, O. N., and Cohen, W. B.: Satellite-based peatland mapping: Potential of the MODIS sensor, Global and Planetary Change, 56, 248–257, https://doi.org/10.1016/j.gloplacha.2006.07.019, 2007.

Proust, S. and Nikora, V. I.: Compound open-channel flows: effects of transverse currents on the flow structure, Journal of Fluid Mechanics, 885, A24, https://doi.org/10.1017/jfm.2019.973, 2020.

Roberts, H., Coleman, J., Bentley, S., and Walker, N.: An embryonic major delta lobe: A new generation of delta studies in the Atchafalaya-Wax Lake Delta system, pp. 690–703, 2003.

Rodgers, J. C., Murrah, A. W., and Cooke, W. H.: The impact of Hurricane Katrina on the coastal vegetation of the Weeks Bay Reserve, Alabama from NDVI data, Estuaries and Coasts, 32, 496–507, http://www.jstor.org/stable/40663559, 2009.

Rogers, K., Kelleway, J. J., Saintilan, N., Megonigal, J. P., Adams, J. B., Holmquist, J. R., Lu, M., Schile-Beers, L., Zawadzki, A., Mazumder, D., et al.: Wetland carbon storage controlled by millennial-scale variation in relative sea-level rise, Nature, 567, 91–95, https://doi.org/10.1038/s41586-019-0951-7, 2019.

Rosen, P. A., Hensley, S., Wheeler, K., Sadowy, G., Miller, T., Shaffer, S., Muellerschoen, R., Jones, C., Zebker, H., and Madsen, S.: UAVSAR: A new NASA airborne SAR system for science and technology research, in: 2006 IEEE Conference on Radar, pp. 8–pp, IEEE, https://doi.org/10.1109/RADAR.2006.1631770, 2006.

Rosso, P., Ustin, S., and Hastings, A.: Use of lidar to study changes associated with Spartina invasion in San Francisco Bay marshes, Remote Sensing of environment, 100, 295–306, https://doi.org/10.1016/j.rse.2005.10.012, 2006.

Saintilan, N., Rogers, K., Mazumder, D., and Woodroffe, C.: Allochthonous and autochthonous contributions to carbon accumulation and carbon store in southeastern Australian coastal wetlands, Estuarine, Coastal and Shelf Science, 128, 84–92, https://doi.org/10.1016/j.ecss.2013.05.010, 2013.

Salter, G., Passalacqua, P., Wright, K., Feil, S., Jensen, D., Simard, M., and Lamb, M. P.: Spatial patterns of deltaic deposition/erosion revealed by streaklines extracted from remotely-sensed suspended sediment concentration, Geophysical Research Letters, https://doi.org/10.1029/2022GL098443, 2022.

Schuerch, M., Spencer, T., Temmerman, S., Kirwan, M. L., Wolff, C., Lincke, D., McOwen, C. J., Pickering, M. D., Reef, R., Vafeidis, A. T., et al.: Future response of global coastal wetlands to sea-level rise, Nature, 561, 231–234, https://doi.org/10.1038/s41586-018-0476-5, 2018.

Shi, Z., Ren, L., Zhang, S., and Chen, J.: Acoustic imaging of cohesive sediment resuspension and re-entrainment in the Changjiang Estuary,
610   East China Sea, Geo-Marine Letters, 17, 162–168, https://doi.org/10.1007/s003670050022, 1997.

Simard, M., Jones, C., Denbina, M. W., Christensen, A., Oliver-Cabrera, T., Liao, T.-H., Fagherazzi, S., Passalacqua, P., Wright, K. A.,
       Zhang, X., et al.: Delta-X, SWOT and NISAR to Revolutionize our Understanding of Coastal Hydrodynamics, in: AGU Fall Meeting
       Abstracts, vol. 2022, pp. B45C–01, 2022.

Slatton, K. C., Crawford, M. M., and Chang, L.-D.: Modeling temporal variations in multipolarized radar scattering from intertidal coastal
615   wetlands, ISPRS journal of photogrammetry and Remote Sensing, 63, 559–577, https://doi.org/10.1016/j.isprsjprs.2008.07.003, 2008.

Spencer, T., Schuerch, M., Nicholls, R. J., Hinkel, J., Lincke, D., Vafeidis, A., Reef, R., McFadden, L., and Brown, S.: Global coastal
       wetland change under sea-level rise and related stresses: The DIVA Wetland Change Model, Global and Planetary Change, 139, 15–30,
       https://doi.org/10.1016/j.gloplacha.2015.12.018, 2016.

Syvitski, J. P., Vo¨ro¨smarty, C. J., Kettner, A. J., and Green, P.: Impact of humans on the flux of terrestrial sediment to the global coastal
620   ocean, science, 308, 376–380, https://doi.org/10.1126/science.1109454, 2005.

Syvitski, J. P., Kettner, A. J., Overeem, I., Hutton, E. W., Hannon, M. T., Brakenridge, G. R., Day, J., Vörösmarty, C., Saito, Y., Giosan, L.,
       et al.: Sinking deltas due to human activities, Nature Geoscience, 2, 681–686, https://doi.org/10.1038/ngeo629, 2009.

Tan, Q., Shao, Y., Yang, S., and Wei, Q.: Wetland vegetation biomass estimation using Landsat-7 ETM+ data, in: IGARSS 2003. 2003
       IEEE International Geoscience and Remote Sensing Symposium. Proceedings (IEEE Cat. No. 03CH37477), vol. 4, pp. 2629–2631, IEEE,
625   https://doi.org/10.1109/IGARSS.2003.1294532, 2003.

Tana, G., Letu, H., Cheng, Z., and Tateishi, R.: Wetlands mapping in North America by decision rule classification using
       MODIS and ancillary data, IEEE Journal of Selected Topics in Applied Earth Observations and Remote Sensing, 6, 2391–2401,
       https://doi.org/10.1109/JSTARS.2013.2249499, 2013.

Thomas, N., Simard, M., Castañeda-Moya, E., Byrd, K., Windham-Myers, L., Bevington, A., and Twilley, R. R.: High-resolution mapping
630   of biomass and distribution of marsh and forested wetlands in southeastern coastal Louisiana, International Journal of Applied Earth
       Observation and Geoinformation, 80, 257–267, https://doi.org/10.1016/j.jag.2019.03.013, 2019.

Twilley, R., Day, J., Bevington, A., Castañeda-Moya, E., Christensen, A., Holm, G., Heffner, L., Lane, R., McCall, A., Aarons, A., et al.:
       Ecogeomorphology of coastal deltaic floodplains and estuaries in an active delta: Insights from the Atchafalaya Coastal Basin, Estuarine,
       Coastal and Shelf Science, 227, 106 341, https://doi.org/10.1016/j.ecss.2019.106341, 2019.

635 Walker, N. D. and Hammack, A. B.: Impacts of winter storms on circulation and sediment transport: Atchafalaya-Vermilion Bay region,
       Louisiana, USA, Journal of Coastal Research, pp. 996–1010, http://www.jstor.org/stable/4300118, 2000.

Wang, F. and D'Sa, E. J.: Potential of MODIS EVI in identifying hurricane disturbance to coastal vegetation in the northern Gulf of Mexico,
       Remote Sensing, 2, 1–18, https://doi.org/10.3390/rs2010001, 2009.

Wang, X., Gao, X., Zhang, Y., Fei, X., Chen, Z., Wang, J., Zhang, Y., Lu, X., and Zhao, H.: Land-cover classification of coastal wetlands
640   using the RF algorithm for Worldview-2 and Landsat 8 images, Remote Sensing, 11, 1927, https://doi.org/10.3390/rs11161927, 2019.

Wang, X., Xiao, X., Zou, Z., Hou, L., Qin, Y., Dong, J., Doughty, R. B., Chen, B., Zhang, X., Chen, Y., et al.: Mapping coastal wetlands of
       China using time series Landsat images in 2018 and Google Earth Engine, ISPRS Journal of Photogrammetry and Remote Sensing, 163,
       312–326, https://doi.org/10.1016/j.isprsjprs.2020.03.014, 2020.

Wdowinski, S., Kim, S.-W., Amelung, F., Dixon, T. H., Miralles-Wilhelm, F., and Sonenshein, R.: Space-based detection of
645   wetlands' surface water level changes from L-band SAR interferometry, Remote Sensing of Environment, 112, 681–696,
       https://doi.org/https://doi.org/10.1016/j.rse.2007.06.008, 2008.

Wdowinski, S., Hong, S.-H., Mulcan, A., and Brisco, B.: Remote-sensing monitoring of tide propagation through coastal wetlands, Oceanography, 26, 64–69, https://doi.org/10.5670/oceanog.2013.46, 2013.

Williams, S. J., Arsenault, M. A., Buczkowski, B. J., Reid, J. A., Flocks, J., Kulp, M. A., Penland, S., and Jenkins, C. J.: Surficial sediment character of the Louisiana offshore Continental Shelf region: a GIS Compilation, Tech. rep., US Geological Survey, https://doi.org/10.3133/ofr20061195, 2006.

Xie, C., Shao, Y., Xu, J., Wan, Z., and Fang, L.: Analysis of ALOS PALSAR InSAR data for mapping water level changes in Yellow River Delta wetlands, International Journal of Remote Sensing, 34, 2047–2056, https://doi.org/10.1080/01431161.2012.731541, 2013.

Yan, Y., Zhao, B., Chen, J., Guo, H., Gu, Y., Wu, Q., and Li, B.: Closing the carbon budget of estuarine wetlands with tower-based measurements and MODIS time series, Global Change Biology, 14, 1690–1702, https://doi.org/10.1111/j.1365-2486.2008.01589.x, 2008.

Zang, Z., Xue, Z. G., Bao, S., Chen, Q., Walker, N. D., Haag, A. S., Ge, Q., and Yao, Z.: Numerical study of sediment dynamics during hurricane Gustav, Ocean Modelling, 126, 29–42, https://doi.org/10.1016/j.ocemod.2018.04.002, 2018.

Zhang, X., Leonardi, N., Donatelli, C., and Fagherazzi, S.: Fate of cohesive sediments in a marsh-dominated estuary, Advances in water resources, 125, 32–40, https://doi.org/10.1016/j.advwatres.2019.01.003, 2019.

Zhang, X., Fichot, C. G., Baracco, C., Guo, R., Neugebauer, S., Bengtsson, Z., Ganju, N., and Fagherazzi, S.: Determining the drivers of suspended sediment dynamics in tidal marsh-influenced estuaries using high-resolution ocean color remote sensing, Remote Sensing of Environment, 240, 111 682, https://doi.org/10.1016/j.rse.2020.111682, 2020.

Zhang, X., Jones, C. E., Oliver-Cabrera, T., Simard, M., and Fagherazzi, S.: Using rapid repeat SAR interferometry to improve hydrodynamic models of flood propagation in coastal wetlands, Advances in Water Resources, 159, 104 088, https://doi.org/10.1016/j.advwatres.2021.104088, 2022a.

Zhang, X., Wright, K., Passalacqua, P., Simard, M., and Fagherazzi, S.: Improving Channel Hydrological Connectivity in Coastal Hydrodynamic Models With Remotely Sensed Channel Networks, Journal of Geophysical Research: Earth Surface, 127, e2021JF006 294, https://doi.org/10.1029/2021JF006294, 2022b.

Zhang, X., Xiao, X., Qiu, S., Xu, X., Wang, X., Chang, Q., Wu, J., and Li, B.: Quantifying latitudinal variation in land surface phenology of Spartina alterniflora saltmarshes across coastal wetlands in China by Landsat 7/8 and Sentinel-2 images, Remote Sensing of Environment, 269, 112 810, https://doi.org/10.1016/j.rse.2021.112810, 2022c.

Zhang, Y., Lu, D., Yang, B., Sun, C., and Sun, M.: Coastal wetland vegetation classification with a Landsat Thematic Mapper image, International Journal of Remote Sensing, 32, 545–561, https://doi.org/10.1080/01431160903475241, 2011.

Zhao, B., Yan, Y., Guo, H., He, M., Gu, Y., and Li, B.: Monitoring rapid vegetation succession in estuarine wetland using time series MODIS-based indicators: an application in the Yangtze River Delta area, Ecological Indicators, 9, 346–356, https://doi.org/10.1016/j.ecolind.2008.05.009, 2009.

Zoffoli, M. L., Kandus, P., Madanes, N., and Calvo, D. H.: Seasonal and interannual analysis of wetlands in South America using NOAA-AVHRR NDVI time series: the case of the Parana Delta Region, Landscape Ecology, 23, 833–848, https://doi.org/10.1007/s10980-008-9240-9, 2008.